



universität
wien

MASTERARBEIT / MASTER'S THESIS

Titel der Masterarbeit / Title of the Master's Thesis

„Investigation of effects of poroelasticity
on seismic wave speed
in Argostoli, Greece“

verfasst von / submitted by

Sophie Authried, BSc

angestrebter akademischer Grad / in partial fulfilment of the requirements for the degree
of

Master of Science (MSc)

Wien, 2022 / Vienna 2022

Studienkennzahl lt. Studienblatt /
degree programme code as it appears on
the student record sheet:

A 066 680

Studienrichtung lt. Studienblatt /
degree programme as it appears on
the student record sheet:

Joint-Masterstudium Physics of the Earth
(Geophysics)

Betreut von / Supervisor:

prof. RNDr. Peter Moczo, DrSc.

I hereby declare I wrote this thesis by myself, only with the help of referenced literature, under the careful supervision of my thesis supervisor.

Acknowledgment

First and foremost, I would like to express my deepest gratitude to my supervisor, Professor Peter Moczo, Academician of the Learned Society of Slovakia, and person responsible for the Joint Master Program Physics of the Earth shared by the Comenius University in Bratislava, Slovakia, and University of Vienna, Austria. His teaching style, admirable enthusiasm and impressive expertise made a strong impression on me throughout the whole time of my study as a Master student. I am truly thankful not only for his continuous support and constant guidance, but also invaluable knowledge and thoughtful insight during my Master study leading to this thesis.

I would also like to greatly acknowledge my consultants and research advisors, MSc. Dávid Gregor, PhD. and doc. Mgr. Martin Gális, PhD. Without their dedicated involvement, supportive assistance, and passionate participation in every step throughout the process of the study, this thesis would not have been accomplished. Discussions with David and Martin have always been very important and illuminating for steering the project in the right direction. Especially when it came to computational challenges, David played an irreplaceable role of developing our program and solving problems in the most efficient way.

Further, I would like to thank Dr. Fabrice Hollender, CEA and ISTERre France, and Zafeiria Roumelioti, Assistant Professor of Seismology-Geophysics, University of Patras, for their collaborative effort of providing necessary data for the study and imparting their knowledge of valuable information about the research site and beyond.

Last but not least, I wish to express my profound gratitude to my family for always believing in me, guiding me through life and providing me with unceasing encouragement to achieve this milestone. I could not have undertaken this journey without them.

Finally, I would like to thank my friends. This accomplishment would not have been possible without their continuous encouragement and unfailing support throughout my years of study and the process of researching and writing the thesis. Thank you.

Preface

One of the main goals of modern earthquake seismology is the prediction of seismic ground motion during future earthquakes, especially in populated earthquake-prone areas. Seismic hazard in numerous urban centers is considerably increased because of their location on top of sedimentary basins or valleys which can cause local site effects – anomalously large or prolonged seismic ground motions due to the interference and resonance of seismic waves in sediment-filled shallow layers.

The near-surface shear wave (S) speed is one of the factors contributing to the site effects and is thus an important parameter for the estimation of ground motion amplitude and the definition of site classification. A sensitivity of S-wave speed to seasonal weather variation i.e., varying rainfall, temperature, and soil moisture, has already been investigated within several research projects and demonstrated by laboratory experiments. In a more practical context of earthquake engineering, it was shown that buildings experience different load under different moisture content of shallow soil during seismic events, and that extended dry periods may lead to greater earthquake ground motion impacts. Especially extreme weather variations, which keep occurring more frequently on a global scale due to climate change, emphasize the great importance of studying and understanding the processes which correlate seasonal weather variations with the variation of S-wave speed and the response of soil.

Biot theory of poroelasticity quantifies the effect of porous fluid saturated soil on seismic wave propagation and earthquake ground motion in heterogenous poroelastic media. Based on this theory, our work presents investigations of poroelastic effects related to the seasonal variation of seismic wave speeds due to rainfall-induced variation of the water content in a near-surface sedimentary layer at one of the most earthquake active sites in Europe (Argostoli, Greece).

Contents

1. Introduction.....	1
1.1. Seismic waves in the poroelastic medium.....	1
1.1.1. Poroelastic medium	1
1.1.2. Biot theory of poroelasticity	3
1.1.3. Gassmann theory	5
1.1.4. Constitutive laws and equations of motion.....	9
1.1.5. Seismic waves in the poroelastic medium.....	11
1.1.6. Velocity dispersion and quality factor relations	12
1.2. Rainfall-induced variation of seismic wave velocity in soil at ARGOSTOLI seismic array NETWORK (ARGONET), Greece.....	15
1.2.1. Geology and geophysical background of Argostoli on Cephalonia Island	15
1.2.2. Geophysical surveys of Argostoli.....	16
1.2.3. Seasonal variation of shear wave velocity found by the ARGONET vertical accelerometric array	18
2. Goals of the Thesis	23
3 Development of a methodology for investigating effects of pore saturation on seismic wave speeds in the top 2m layer at the ARGONET vertical array	25
3.1. Estimation of poroelastic parameters	25
3.2. The Neighbourhood Algorithm	27
3.2.1. Limit values of parameter space.....	29
3.2.2. Misfit function of seismic constrained and predicted data	30
3.2.3. Control parameters	31
3.2.4. Random number generation.....	33
3.2.5. Visualization of the search for an optimal solution in the parameter space using the NA	33
3.3. Terminology of parameters in our study	35
4. Poroelastic models of the top 2m layer	39
4.1. Determination of seismic parameters for dry and wet seasons	39

4.2. Poroelastic Inversion for the dry season	41
4.2.1. Choices of input parameter sets	41
4.2.2. Determination of models.....	47
4.3. Poroelastic inversion for the wet season	54
4.3.1. Choices of input parameter sets	54
4.3.2. Determination of models.....	59
5. Conclusions.....	65
REFERENCES	67
ABSTRAKT	73
ABSTRACT.....	75

1. Introduction

1.1. Seismic waves in the poroelastic medium

1.1.1. Poroelastic medium

Earthquake ground motion and seismic wave propagation are usually simulated in an adequate way using an elastic or viscoelastic medium inside a target volume of the Earth as material model. However, shallow subsoil layers and rocks of the Earth are generally inhomogeneous on a microscopic scale due to their composition of different material types. Such composite materials can be represented by a fluid-saturated porous medium defined as poroelastic material formed by two phases. A porous material is defined as a solid with pores that is consisting of a solid phase (denoted by subindex “s”), which constitutes the matrix (“m”) of the porous medium, and a fluid phase (“f”), which fills the interconnected pores of the matrix. Various mineral types (e.g., feldspar, quartz, mica) of different grain sizes going from 0.1 to 1 mm can form a collection of particles constituting the solid matrix of a porous rock. Water, air, brine, oil, methane gas or a mixture of these substances are examples of what the fluid phase is typically made of. Illustrations of porous materials are represented in Figure 1.

The study site of this thesis with its material composition, which is located on Cephalonia Island, Greece, is described in more detail in section 1.2. It is characterized by its proximity to the coastline leading to a relatively shallow water table at a depth of 2 m. When investigating the site’s surface sedimentary structures, we distinguish between the saturated zone representing an unconfined groundwater aquifer and the overlaying unsaturated zone. Below the depth of the water table separating both zones, any pores within rocks and between sediments are fully filled by water or brine. Above the depth of the water table, data confirm that this zone contains partially or fully water saturated sedimentary rocks. The water content seems to be affected by the amount of water penetrating throughout the rainy season. There are three types of water content which can be distinguished (Dr. Fabrice Hollender, CEA France – personal communication):

- *Bound water* is the water which remains in the soil even in a dry period due to its strong linkage to the soil elements (especially clay-like elements).
- *Capillary water* is the water which remains in the pores and can be evaporated depending on the evaporation potential, which itself depends on parameters like

temperature. Its relatively low linkage to soil elements allows evaporation but keeps it from draining to the water table.

- *Gravity water* is the water which can circulate within the pores of the unsaturated zone. Due to gravity, this type of water can drain down to the water table within a time range of a few hours.

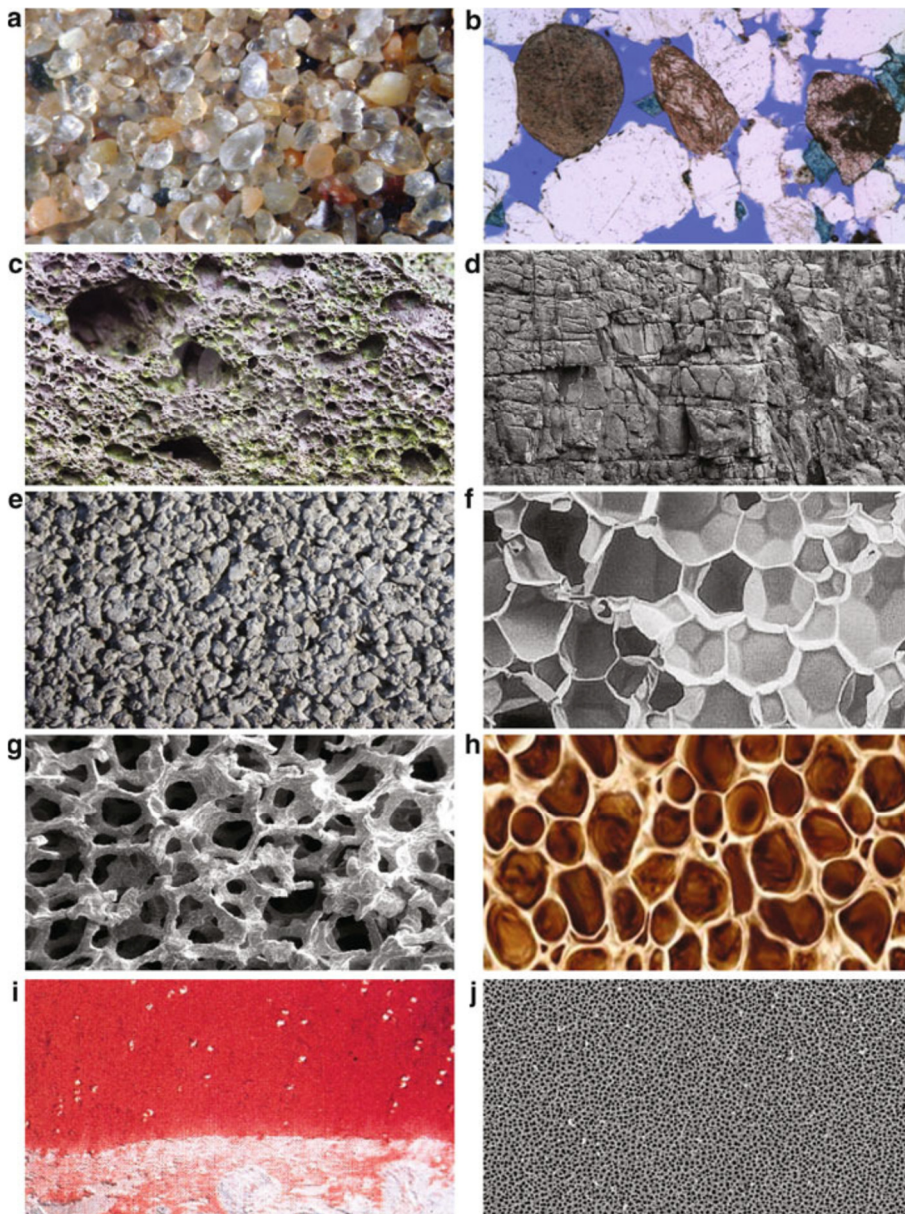


Figure 1. Poroelastic materials reproduced from the book Poroelasticity by Cheng (2016).

Rocks: **a** sand, **b** sandstone, **c** volcanic rock, **d** fractured rock.

Technical materials: **e** pervious concrete, **f** polyurethane foam, **g** metal foam, **j** nanoporous alumina.

Human body: **h** bone with osteoporosis, **i** articular cartilage.

Looking at the physical behavior of poroelastic materials constituting such saturated and unsaturated sedimentary layers, there are two basic phenomena. First, solid to fluid coupling, which appears when a change in fluid mass or fluid pressure in the pores is caused by a change in applied stress. Secondly, fluid to solid coupling, which appears when a change in volume of the porous material is caused by the change of fluid mass or fluid pressure in the pores.

1.1.2. Biot theory of poroelasticity

There are sophisticated theories which define rocks as poroelastic materials by considering them as media with pores partially or fully saturated by fluids. We distinguish two approaches of investigating seismic wave propagation in poroelastic materials. While the first one is based on fundamentals of continuum mechanics (Biot 1956a), the second one is based on a homogenization procedure (Auriault 1980). For the study presented in this thesis, we use Biot's traditional theory which is still widely used and accepted in the field of modelling seismic wave propagation in porous media.

The theory treats the material as continuum. Therefore, characteristics as e.g., the exact atomic structure of the material can be neglected. If this were not the case, fluid and solid phases would have to be treated separately, and the exact geometry and location of the pores in the material would have to be known. This is especially in the fields of seismology, where we look at large areas of investigation, not realistic. As a result, Biot theory of poroelasticity can be considered, which is based on principles of continuum mechanics, linear elasticity of the material and porous medium flow i.e., Darcy flow (Cheng 2016).

Biot was the first to analyze the propagation of waves in poroelastic materials, which are saturated by compressible viscous fluids, in various classical papers (e.g., Biot 1956a, Biot 1956b, Biot 1962a, Biot 1962b). Subsequently, his theory was confirmed experimentally by Plona (1980) and has mainly been utilized within the fields and purposes of the petroleum industry. There it is used to determine physical rock properties inside reservoirs and perform seismic surveys providing accurate results for several investigations. The main assumptions of Biot theory of poroelasticity can be summarized as follows.

- a. *Particle velocities, displacements and strains are small.* Consequently, Eulerian and Lagrangian formulations do not have to be distinguished while dissipation forces, constitutive laws and kinetic momenta are linear.

- b. *The wavelength of seismic waves is large compared to the radius of the pores.*
This is a necessary requirement to apply the theory of continuum mechanics and an implication that scattering dissipation is neglected.
- c. *The liquid phase is continuous.* This means that pores within the porous material are connected, and disconnected pores are part of the matrix.
- d. *The porous medium is fully saturated. The material of the matrix and permeability are isotropic.*
- e. *Thermo-mechanical and chemical effects are not present.*

From fundamental physics and elasticity mechanics most of the basic poroelastic quantities are already known. Additional parameters as porosity, tortuosity, permeability, electrical formation factor, weighted pore volume to grain surface ratio and other related quantities shall be defined herein.

Porosity ϕ is defined as

$$\phi = \frac{V_f}{V_t} \quad (1.1)$$

where V_f is the volume of the fluid, V_s the volume of the solid and

$$V_t = V_f + V_s \quad (1.2)$$

the total volume of the porous material. Since we consider full saturation, the fluid volume equals the volume of the pore space.

Tortuosity T measures the twistedness of the pore channels due to the flow of the fluid not strictly following the pore pressure gradient but being constrained to follow the pore channel network. As a consequence of the „tortuous“ path of the pore connection, this intrinsic property of a porous material is typically defined as the ratio between the actual flow path length and the minimum straight distance between the two ends of the flow path. Therefore, $T \geq 1$ and e.g., for sandstone T is usually in the range of 2–3.

Intrinsic (hydraulic) permeability κ_0 measures the ability of a porous material to transmit fluids. It was first defined by Darcy specifically in the case of water by showing that the flow rate per unit area is proportional to the pressure drop in the porous medium. Since the property is treated as area, its SI-unit is m^2 . The traditionally used unit for permeability in geophysical applications is *Darcy* = $0.986923 \times 10^{-12} m^2$.

Parameter n_J is defined as

$$n_J = \frac{\Lambda^2}{F \kappa_0} \quad (1.3)$$

where length Λ represents a weighted pore volume to grain surface ratio (Masson *et al.* 2006) and the electrical formation factor F represents the ratio between the resistivities of the fluid-saturated rock and the pore fluid (Gist 1994). While for clean sands a value of $n_J = 8$ is consistent with both laboratory and numerical experiments, for shaly sands the value is $n_J \ll 8$. In the applications of Pride *et al.* (2004), Barros & Dietrich (2008) and Yang & Mao (2017) $n_J = 8$ was used. As Pride (2005) states in his work, the value of $n_J = 8$ can conveniently be applied as modelling choice for various materials including unconsolidated materials and clean sandstones. Furthermore, it is the theoretically expected result for cylindrical tube models of the pore space.

1.1.3. Gassmann theory

To quantify how porosity, mineral composition, and fluid saturation is affecting seismic parameters e.g., wave speeds or average bulk density of the medium, a combination of empirical relations and theoretical formulations is necessary. When it comes to modeling the effect of fluid saturation, empirical relations generally struggle since they are not based on physical principles (Smith *et al.* 2003). Therefore, the most commonly applied theoretical approach to quantify the effect of fluid saturation is provided by the Gassmann theory (Gassmann 1951). Gassmann introduces the following equation

$$K_u = K_m + \frac{\left(1 - \frac{K_m}{K_s}\right)^2}{\frac{\phi}{K_f} + \frac{(1-\phi)}{K_s} - \frac{K_m}{K_s^2}} \quad (1.4)$$

relating the saturated bulk modulus of the rock (undrained of pore fluids) K_u to the rock's porosity ϕ , the bulk modulus of the porous matrix K_m , the bulk modulus of the rock's solid phase K_s and the bulk modulus of the fluid filling the pores K_f .

Since Gassman's relation is based on assumptions of Biot theory of poroelasticity, the combination of both is oftentimes also denoted as Biot-Gassmann-Theory („BGT“). The application of Gassmann's relation requires several assumptions additional to the ones prescribed by Biot theory (Smith *et al.* 2003):

- a) *The matrix is composed of ideantical grains.* If the rock's matrix were composed of multiple mineral types, the assumption of a homogeneous, isotropic rock with completely connected pore spaces within the mineral would be violated.
- b) *The equation is only valid at low frequencies.* This implies an equilibrated pore pressure throughout the rock and over a length scale big relative to the pore scale and small relative to the wavelength of the passing seismic wave.
- c) *The pores are saturated with one single or one effective fluid phase.*

The last assumption implies that the porous medium does not necessarily need to be fully saturated by one single fluid phase (e.g., water) as originally prescribed by Biot's traditional theory. Instead, a mixture of multiple fluids (e.g., water with air) can build a homogeneous effective fluid phase, uniformly distributed throughout the pore space.

This indicates that effective fluid phase parameters must be introduced within the BGT. Such parameters represent the simplest approach to consider partially saturated media with several fluid phases in case of a uniform saturation. They can be found by weighted or harmonic averages using volume fractions of the considered fluid phases. In this work the effective fluid in the pores represents a mixture of air (denoted as "a") and water ("w") where S_a and S_w denote the corresponding volume fractions of the two fluid phases:

$$S_a + S_w = 1 \quad (1.5)$$

Let ρ_a and ρ_w be the densities of the air and water, respectively. The effective fluid density ρ_f is then given by a weighted arithmetic average (Voigt *et al.* 1889)

$$\rho_f = S_a \rho_a + S_w \rho_w \quad (1.6)$$

while the average bulk density of the material is given by

$$\rho = (1 - \phi) \rho_s + \phi \rho_f \quad (1.7)$$

where ρ_s represents the density of the solid constituting the matrix of the porous medium.

The effective fluid bulk modulus K_f is calculated according to Brie *et al.* (1995) and Carcione *et al.* (2006) as

$$K_f = (K_w - K_a) (S_w)^e + K_a \quad (1.8)$$

where e represents the Brie exponent. The value is typically set to $e = 5$ as suggested by Carcione *et al.* (2006) to gain satisfying agreement with experimental findings of Johnson (2001).

The effective viscosity η is calculated according to Teja and Rice (1981) as

$$\eta = \eta_a \left(\frac{\eta_w}{\eta_a} \right)^{(1-S_a)} \quad (1.9)$$

The BGT assumes that the shear modulus of the solid matrix is insensitive to the composition of the pore filling fluid. Therefore, drained μ_m and undrained μ_u shear moduli of the matrix are equal

$$\mu_u = \mu_m \quad (1.10)$$

while the bulk modulus of the solid matrix K_m may be dependent on the fluid content.

The above defined effective fluid parameters are part of the fundamental poroelastic material parameters

$$\{\rho_s, K_s, \rho_f, K_f, \eta, K_m, \mu_m, \phi, T, \kappa_0, n_J\} \quad (1.11)$$

These 11 parameters in addition to some of their interdependencies can be found in Table 1.

Table 1. Fundamental poroelastic material parameters
(modified from Gregor *et al.* 2020).

Symbol	Name	Units	Relation
solid phase			
ρ_s	density	kg / m^3	
K_s	bulk modulus	Pa	
μ_s	shear modulus	Pa	
effective fluid phase			
ρ_f	density	kg / m^3	$S_a \rho_a + S_w \rho_w$
K_f	bulk modulus	Pa	$(K_w - K_a)(S_w)^e + K_a$
η	dynamic viscosity	$Pa s$	$\eta_a (\eta_w / \eta_a)^{(1-S_a)}$
solid matrix (drained)			
K_m	bulk modulus	Pa	
μ_m	shear modulus	Pa	
λ_m	Lamé elastic coefficient	Pa	2D: $K_m - \mu_m$
			3D: $K_m - 2\mu_m/3$
ϕ	porosity		V_f / V_t
T	tortuosity		
κ_0	intrinsic permeability	m^2	
saturated porous medium (undrained)			
ρ	average bulk density	kg / m^3	$(1 - \phi) \rho_s + \phi \rho_f$
K_u	bulk modulus	Pa	$K_m + \alpha^2 M$
λ_c	Lamé coefficient	Pa	2D: $K_u - \mu_m$
			3D: $K_u - 2\mu_m/3$
α	coefficient of effective stress		$1 - K_m / K_s$
M	coupling modulus between solid and fluid	Pa	$\frac{K_s}{1 - \phi - K_m / K_s + \phi K_s / K_f}$
m	mass coupling coefficient	kg / m^3	$T \rho_f / \phi$
b	resistive damping (friction)	$Pa s / m^2$	η / κ_0
f_c	Biot characteristic frequency	Hz	$\phi \eta / 2\pi T \rho_f \kappa_0$
F	electrical formation factor		$T / \phi = m / \rho_f$
Λ	weighted pore-volume to grain-surface ratio	m	
n_J	dimensionless parameter		$\Lambda^2 / F \kappa_0$
Ω	auxiliary material parameter	Hz	$n_J \pi f_c / 2$

1.1.4. Constitutive laws and equations of motion

Results and formulas of the following subsections are derived and provided by Carcione (2015).

Summary of constitutive laws of a poroelastic medium

Displacement and strain are described as macroscopic averages in Biot theory. They are quantities specified for a macroscopic elementary volume. Therefore, stresses are defined as forces acting per unit area including the solid matrix and fluid phase within the poroelastic material. Consequently, macroscopic averages of stresses acting in the fluid and matrix can be distinguished.

The following stress-strain-relations for an elastic matrix include σ_{ij} as stress tensor, $\varepsilon_{kk}^{(m)}$ as strain tensor (“m” referring to matrix), μ_m as shear modulus of the solid matrix, M as coupling modulus between solid and fluid, α as poroelastic coefficient, p as fluid pressure and λ_m as Lamé coefficient. All parameters are also listed and defined in Table 1.

$$\begin{aligned}\sigma_{ij} &= \lambda_m \varepsilon_{kk}^{(m)} \delta_{ij} + 2\mu_m \varepsilon_{ij}^{(m)} - \alpha p \delta_{ij} \\ p &= -\alpha M \varepsilon_{kk}^{(m)} - M \varepsilon_{kk}^w\end{aligned}\tag{1.12}$$

These constitutive laws of poroelastic materials (1.12) can be generalized to stress-strain-relations of poroviscoelastic materials, which also consider the viscoelasticity of the solid matrix and thus attenuation due to it. In this work we only consider Biot’s poroelastic equations for materials with an elastic solid matrix.

Summary equations of motion of a poroelastic medium

The following equations of motion include ρ as average bulk density, ρ_f as fluid density, v_i as solid particle velocity, q_i as fluid particle velocity relative to the solid, p as fluid pressure, σ_{ij} as stress tensor, η as dynamic viscosity, κ_0 as intrinsic permeability, Ω as auxiliary parameter and m as mass coupling coefficient. All parameters are also listed and defined in Table 1.

$$\begin{aligned}\rho \frac{\partial v_i}{\partial t} &= \frac{\partial \sigma_{ij}}{\partial x_j} - \rho_f \frac{\partial q_i}{\partial t} \\ m \frac{\partial q_i}{\partial t} &= -\frac{\partial p}{\partial x_i} - \rho_f \frac{\partial v_i}{\partial t} - b q_i\end{aligned}\tag{1.13}$$

The first equation in (1.13) represents the Biot-Euler dynamical equation, where the first two terms are well known from the equations of motion for the elastic continuum. The third term represents a correction term. It includes the relative wave-induced motion of the fluid with respect to the walls of the pore space (fluid flow, Biot flow or macroscopic flow). The second equation in (1.13) represents the generalized dynamic Darcy's Law for fluid flow in the pores induced by passing waves creating pressure gradients within the fluid.

When wave propagation through a porous material occurs, fluid flow is accompanied by friction between the solid matrix and viscous fluid. This causes a viscous energy loss resulting in attenuation of the passing waves. Fluid flow and corresponding friction persist until the pore pressure is equilibrated. Due to its kinetic nature, this attenuation is represented in the equation of motion by the resistive friction term b .

With its significantly different behavior at low and high frequencies, fluid flow is considered as frequency dependent phenomenon. Therefore, two frequency regimes need to be distinguished. Biot characteristic frequency f_c was introduced to quantitatively characterize the low-frequency (LF) and high-frequency (HF) regime. At sufficiently low frequencies (i.e., $f \ll f_c$) the HF effects can be neglected. f_c is defined as

$$f_c = \frac{\phi \eta}{2\pi T \rho_f \kappa_0} = \frac{1}{2\pi T} \frac{\phi}{\rho_f} b\tag{1.14}$$

Dynamic viscosity η and intrinsic (hydraulic) permeability κ_0 are the two parameters f_c is mostly affected by. This is due to their possibility to change in relatively high orders e.g., κ_0 in orders of magnitude, compared to the remaining parameters e.g., T ranging between 1–2.

The model describing the fluid flow with constant permeability $\kappa = \kappa_0$ and constant resistive friction $b = \eta / \kappa_0$ is often called Biot model, according to the work of Biot (1956a). Since the fluid flow in the HF regime cannot be properly described by Biot model, the constant resistive friction in Darcy's Law must be replaced by the frequency dependent resistive friction $b(\omega) = \eta / \kappa(\omega)$.

To connect the LF and HF behaviors of the fluid, Johnson *et al.* (1987) used a complex permeability function. The model for the frequency dependent (dynamic) permeability $\kappa(\omega)$ (1.15) and frequency dependent friction $b(\omega)$ is called JKD model (according to the names Johnson, Koplik and Dashen). $\kappa(\omega)$ can be written as

$$\kappa(\omega) = \kappa_0 \left[\frac{1}{\sqrt{\Omega}} \sqrt{\Omega + i\omega} \right]^{-1} \quad (1.15)$$

where Ω is an auxiliary parameter

$$\Omega = \frac{n_J \omega_c}{4} \quad (1.16)$$

and Biot characteristic angular frequency is $\omega_c = 2\pi f_c$. The limit of $\kappa(\omega)$ for $\omega \rightarrow 0$ converges to κ_0 .

1.1.5. Seismic waves in the poroelastic medium

Biot predicted the existence of two compressional waves and one shear wave by assuming that the fluid may cause friction if it flows relatively to the solid matrix. The first longitudinal wave is typically denoted as fast P-wave. It behaves similarly to the already known P-wave in an elastic medium, characterized by a comparatively large phase velocity, low attenuation, and very small dispersion. The shear wave also behaves similarly to the already known S-wave in an elastic medium, characterized by a similar degree of attenuation and dispersion as the fast P-wave. The second longitudinal wave is typically denoted as slow P-wave (or Biot slow wave) and distinguishes the poroelastic wavefield from the elastic one. It has a comparatively low phase velocity, high attenuation, and strong dispersion especially at low frequencies. While the fast P-wave is accompanied by in-phase compressional motion of fluids and solids, the slow P-wave is accompanied by out-of-phase motions.

As mentioned, the existence of the slow P-wave in addition to the common fast P-wave and S-wave constitutes the main difference between the elastic or viscoelastic medium and the poroelastic medium. When all seismic waves propagate through the poroelastic medium, dynamic viscosity of the fluid causes dissipation and slight velocity dispersion in the fast P- and S-waves, and a strong velocity dispersion in the slow P-wave. Therefore, the slow P-wave behaves mostly as diffusive wave. Thereby, we distinguish between source frequencies smaller than Biot characteristic frequency f_c characterizing the LF

regime and source frequencies above f_c characterizing the HF regime. In the LF regime the slow P-wave is associated with a diffusion process and can only significantly be seen near material heterogeneities or very close to the seismic source. In the HF regime it can propagate to larger distances. Though in low permeable materials with high clay content, this mode is also diffusive above f_c , which is pointed out in Carcione *et al.* (2010).

In contrast to this slow wave behavior, the fast P- and S-wave are usually only lightly attenuated over the whole frequency range and typically indistinguishable from those of the viscoelastic wavefield, at least over short distances. In LF regimes and long distances from the source the slow P-wave is not observable due to its high attenuation. Therefore, the wave types propagating through poroelastic media within a homogenous poroelastic model in the LF regime are almost indistinguishable from those in a single-phase viscoelastic medium. This was demonstrated by Carcione (1998) and Lemoine (2013).

1.1.6. Velocity dispersion and quality factor relations

To investigate and characterize how waves propagate through a porous medium, the medium can be penetrated by plane waves. Due to isotropy of the medium, compressional and shear waves are decoupled from each other. The exact derivation of the dispersion equations for different wave types can be found in Carcione (2015).

Velocity dispersion of compressional waves

First, Carcione applies the divergence operation to the equations of motion assuming constant material properties. Then relations for total stress components, average density and variation of the fluid content are inserted. Without loss of generality plane waves are considered

$$v_m = v_{m0} \exp[i(2\pi f t - kx)] \quad (1.17)$$

$$v_f = v_{f0} \exp[i(2\pi f t - kx)] \quad (1.18)$$

where the complex wave number is denoted as k . These wave equations are now substituted into the equations of motion, which leads to a system of two equations constituting an eigenvalue/eigenvector problem. To obtain the dispersion relation the determinant of the system is set equal to zero

$$-\left(\rho_f^2 + \frac{i}{2\pi f} \hat{Y}(f) \rho\right) v_c^4 + \left[\frac{i}{2\pi f} \hat{Y}(f) (\lambda_c + 2\mu_m) + M(2\alpha\rho_f - \rho)\right] v_c^2 + M(\lambda_m + 2\mu_m) = 0 \quad (1.19)$$

The phase velocity of the fast P-wave, VP_{fast} , and slow P-wave, VP_{slow} , are obtained by solving (1.19), where $\hat{Y}(f)$ has two forms corresponding to the different physical models of friction (Biot and JKD):

$$\hat{Y}(f) = \begin{cases} i2\pi f m + b \\ i2\pi f m + b(\omega) \end{cases} \quad (1.20)$$

The first option refers to Biot model with constant resistive friction, the second option refers to JKD model with frequency dependent resistive friction.

The two resulting roots of the solution of (1.19) in v_c^2 correspond to the two longitudinal poroelastic waves, VP_{fast} and VP_{slow} . The respective complex velocities can be denoted by $v_{c\pm}$ referring to the two possible signs of the resulting square root of the solution.

Velocity dispersion of the shear wave

First Carcione applies the curl operator to the equations of motion using the relation for variation of the fluid content and assuming constant material properties. Inserting them in relations for deviator, stress component and average density simplifies the equations. Additionally, the curl of the strain-energy density expression is used. Without loss of generality plane waves are considered

$$\Omega^{(m)} = \Omega_{m0} \exp[i(2\pi f t - kx)] \quad (1.21)$$

$$\Omega^{(f)} = \Omega_{f0} \exp[i(2\pi f t - kx)] \quad (1.22)$$

These wave equations are now substituted into the equations of motion, which leads to a system of two equations

$$\left[\mu_m - v_s^2(1-\phi)\rho_s\right] \Omega_{m0} - \phi\rho_f v_s^2 \Omega_{f0} = 0 \quad (1.23)$$

$$-\left(\rho_f + \frac{1}{2\pi f} \hat{Y}\phi\right) \Omega_{m0} + \left(\frac{i}{2\pi f} \hat{Y}\phi\right) \Omega_{f0} = 0 \quad (1.24)$$

where $v_s = 2\pi f/k$ represents the complex shear wave velocity. The solution is obtained as

$$v_s(f) = \sqrt{\frac{\mu_m}{\rho - i2\pi f \rho_f^2 \hat{Y}^{-1}(f)}} \quad (1.25)$$

corresponding to the poroelastic shear wave velocity VS .

Consequently, all three final poroelastic phase velocities $VP_{fast}(f)$, $VP_{slow}(f)$ and $VS(f)$ can be obtained by

$$VP_{fast}(f) = \left[\text{Re}\{v_{c+}^{-1}(f)\} \right]^{-1} \quad (1.26)$$

$$VP_{slow}(f) = \left[\text{Re}\{v_{c-}^{-1}(f)\} \right]^{-1} \quad (1.27)$$

$$VS(f) = \left[\text{Re}\{v_s^{-1}(f)\} \right]^{-1} \quad (1.28)$$

All above defined dispersion relations do not only contain some of the fundamental poroelastic parameters (1.11) but also parameters, which can be derived from these fundamental ones e.g., resistive friction b . All fundamental parameters and their interdependencies can be found in Table 1.

Quality factor relations

The attenuation due to friction between the viscous fluid and solid matrix for the slow P-wave, fast P-wave and S-wave is quantified by the inverse quality factor Q^{-1} . It is calculated using the complex velocities and can be found by

$$QP_{fast}^{-1}(f) = \frac{\text{Im}\{v_{c+}^2(f)\}}{\text{Re}\{v_{c+}^2(f)\}} \quad (1.29)$$

$$QP_{slow}^{-1}(f) = \frac{\text{Im}\{v_{c-}^2(f)\}}{\text{Re}\{v_{c-}^2(f)\}} \quad (1.30)$$

$$QS^{-1}(f) = \frac{\text{Im}\{v_s^2(f)\}}{\text{Re}\{v_s^2(f)\}} \quad (1.31)$$

1.2. Rainfall-induced variation of seismic wave velocity in soil at ARGOSTOLI seismic array NETWORK (ARGONET), Greece

1.2.1. Geology and geophysical background of Argostoli on Cephalonia Island

In the Mediterranean region, western Greece belongs to the main active tectonic areas with the highest seismic activity in Europe. The island of Cephalonia is located at the northernmost edge of the Hellenic arc (Figure 2) and at the boundary of the Eurasian and African plates, which converge with a rate of up to 35 mm/yr . The subduction of the Mediterranean lithosphere abruptly stops right at the Cephalonia Transform Fault Zone (CTFZ).

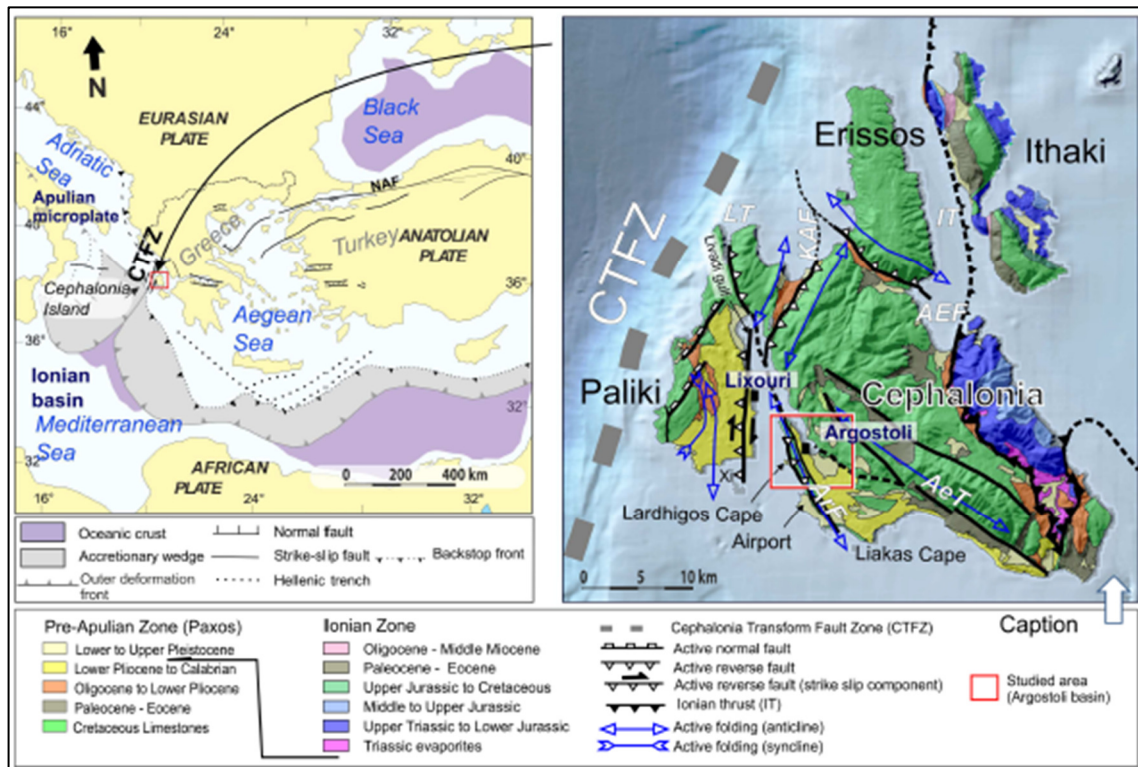


Figure 2. Geographical, geophysical, and geological maps of the area.

(Reproduced from Cushing *et al.* 2020 and modified by Theodoulidis *et al.* 2018a)

Left: Geodynamic map of the wider south-eastern Mediterranean region with fault zones.

Right: Geology and prevailing seismotectonic features of the Cephalonia and Ithaca Island.

The seismic hazard at this north-western end of the Aegean subduction frontal thrust is very high. The earthquake in 1953 specifically affected the island in terms of a seismic uplift of its southern part up to one meter (Cushing *et al.* 2020). It measured a seismic

moment magnitude of $M_w = 7.3$ and caused substantial damage in the island's capital, Argostoli, which had to be rebuilt completely. A sequence of earthquakes in 2014 including two seismic events of $M_w = 6$ led to the maximum ever recorded peak ground acceleration (PGA) in Greece (Theodoulidis *et al.* 2016).

To study the basin, a first vertical accelerometer network (Ionianet) was installed by the National Technical University of Athens in the 1990's (Protopapa *et al.* 1998). Based on ensuing observations, the Plio-Quaternary Koutavos-Argostoli basin site was selected by the French Research Agency PIA SINAPS@ project in 2011 to conduct a first survey (Berge-Thierry *et al.* 2017, Berge-Thierry *et al.* 2019). In 2015 the ARGOSTOLI seismic array NETWORK (ARGONET) was established in the Koutavos area. Four boreholes were drilled, and several accelerometers were installed on surface and different depths creating high quality datasets (Theodoulidis *et al.* 2018a).

The analysis of rotation sensor data from the SINAPS (Sbaa *et al.* 2017) and the spatial coherency analysis of seismic ground motions (Svay *et al.* 2017, Imtiaz *et al.* 2018) are exemplary studies which were carried out using data given by the installed seismic arrays. Cushing *et al.* (2020) and Roumelioti *et al.* (2020) present results of geological, geophysical, and geotechnical investigations based on ambient vibration measurements for horizontal-to-vertical spectral ratio (HVSr) analysis and surface-wave dispersion analysis (SWDA).

Today, Argostoli is one of the most earthquake active and monitored sites in Europe and its seismic monitoring provides unprecedented and unique data.

1.2.2. Geophysical surveys of Argostoli

In September 2013 and October 2017, two geophysical surveys were carried out. Thus, shear wave velocity was measured and new information about the geometry of the Argostoli basin could be obtained. Thereby, single station ambient vibration measurements for HVSr analysis (Nakamura 1989; SESAME team 2004; Bard *et al.* 2010), and SWDA technique were involved (Foti *et al.* 2018). Six areas were investigated by Ambient Vibration Arrays shown in Figure 3 and denoted as *Array 1* (rock site), *Array 2* (Pliocenesite), *Array 3* (west of Koutavos), *Array 4* (center of Koutavos), *Array 5* (ARGONET) and *Array 6* (Large array).

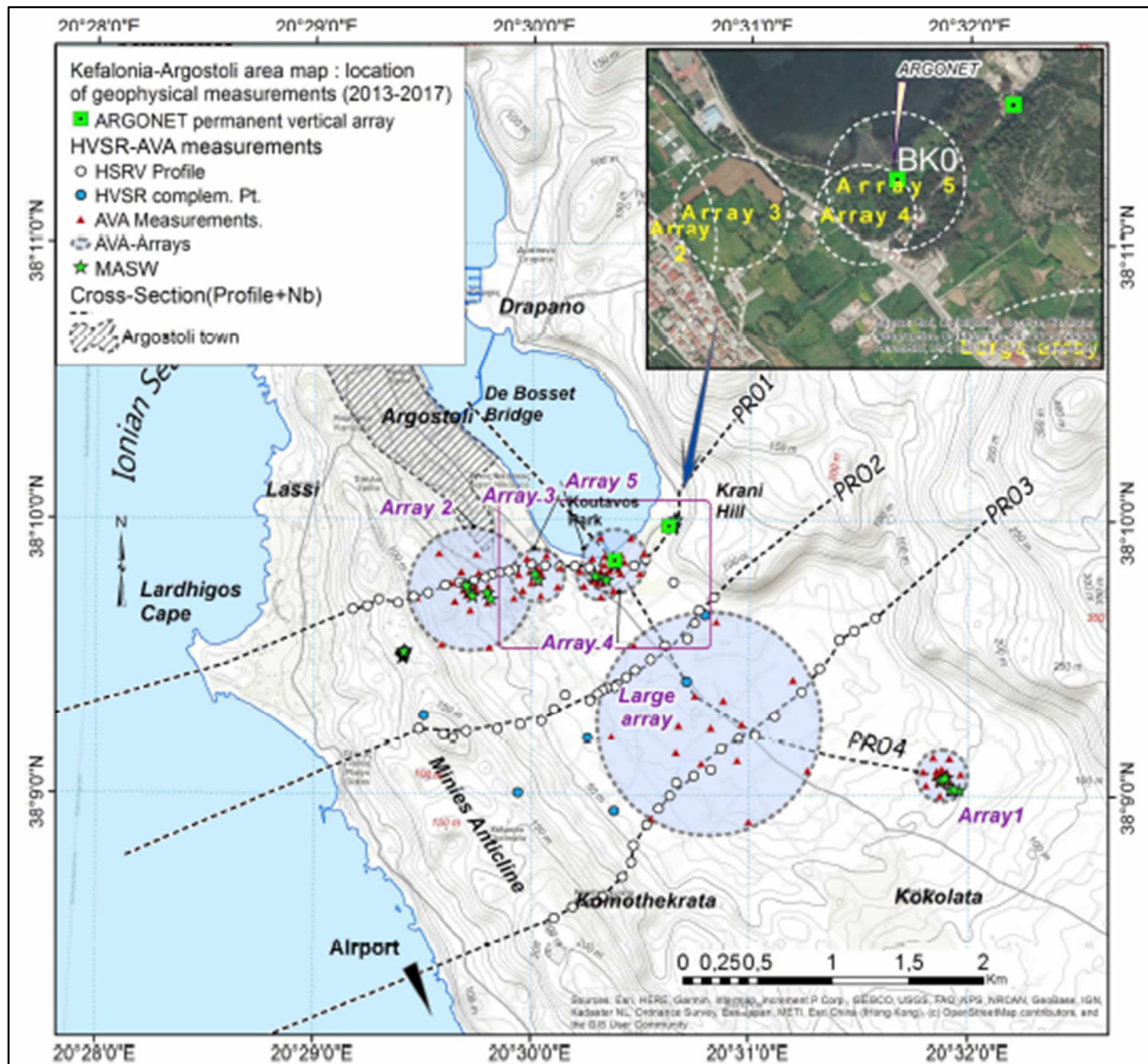


Figure 3. Map with location of SWDA measurements and Ambient Vibration Arrays (HVSRA and MASW) during geophysical surveys in 2013 and 2017 with three profiles (PR01, PR02, PR03), along which HVSRA were performed. Indication where the permanent ARGONET sensor array (vertical array with free field station on bedrock) is located. (Reproduced from Cushing *et al.* 2020).

Six Ambient Vibration Arrays: *Array 1* (rock site), *Array 2* (Pliocene site), *Array 3* (west of Koutavos), *Array 4* (center of Koutavos), *Array 5* (ARGONET) and *Array 6* (Large array).

The SWDA consists of measuring the phase velocity of surface Rayleigh and/or Love waves as a function of frequency to acquire the dispersion curves. By using an inversion algorithm, the dispersion curves are inverted to shear wave profiles.

The HVSRA method includes the computation of Fourier spectra of ambient vibration measurements and creating plots of the horizontal to vertical spectra ratio. Since this analysis is done over multiple time windows, a mean is computed to provide the final HVSRA curve. The analyses were carried out along three profiles shown in Figure 3 (PR01, PR02, PR03).

1.2.3. Seasonal variation of shear wave velocity found by the ARGONET vertical accelerometric array

1.2.3.1. The ARGONET vertical accelerometric array

Array 5 was deployed with the ARGONET accelerometric station in the southeast of Argostoli, which was installed in July 2015. Primarily, it consisted of one surface accelerometric station (CK0) which was mounted on a concrete slab inside a wooden shelter pictured in Figure 4 (a), and three stations (CK15, CK40, CK83) at depths of 15.5 m, 40.1 m and 83.4 m with an interborehole distance of 3 m (Theodoulidis *et al.* 2018a). In 2016 an additional borehole station (CK6) at depth of 5.6 m was installed and put into operation. All five three-component sensors are recorded at the rate of 200 samples per second by Nanometrics digitizers.

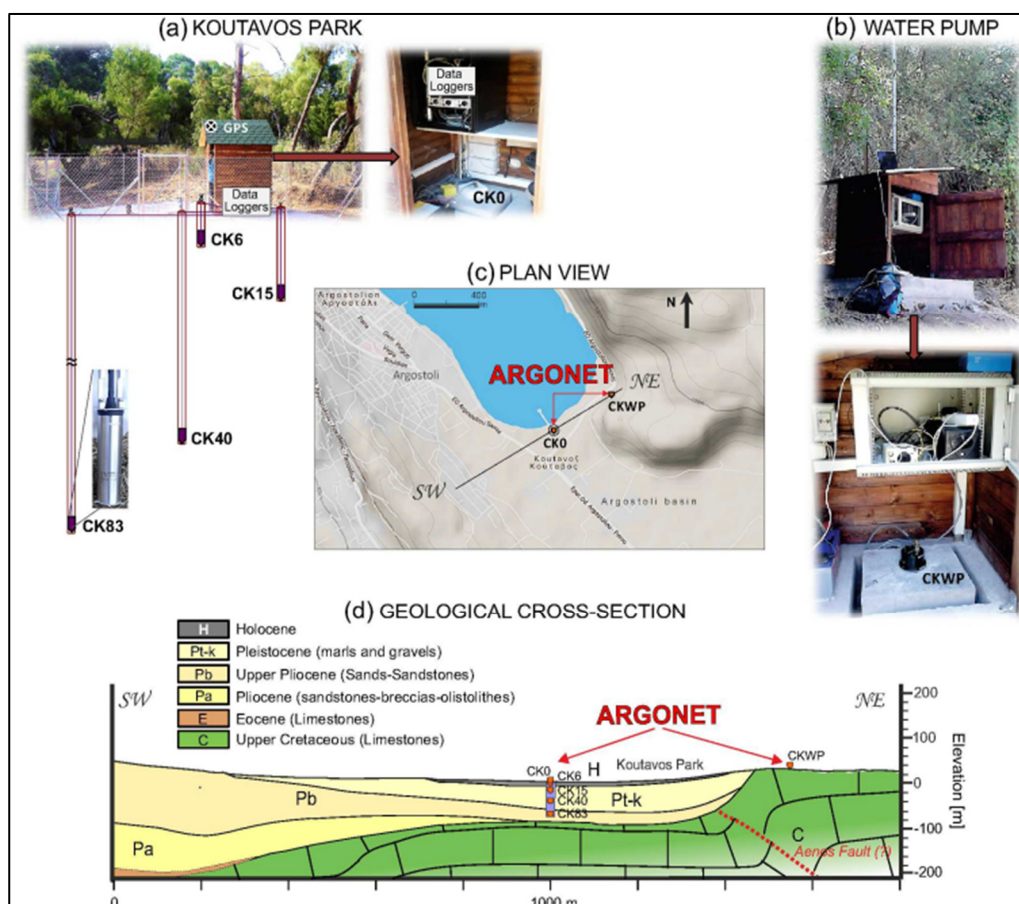


Figure 4. Array configuration of (a) ARGONET surface accelerometric station (CK0) with four borehole stations at different depth levels (CK6 at 5.6m, CK15 at 15.5 m, CK40 at 40.1 m, CK83 at 83.4 m) in Koutavos Park and a (b) free-field station (CKWP) on bedrock 440 m away from CK0, seen in (c) plan view from above and as (d) geological cross-section from the side. (Reproduced from Theodoulidis *et al.* 2018a).

Array 5 is located within Kaóutavous Park with an outcropping Holocene formation (H). Geological and geotechnical observations showed that the top 2m-layer of the soil column consist of artificial deposits (sandy and silty gravel). Underneath, a 6m thick zone of lagoon deposits (silty sands, sandy silts, and clays) can be found overlaying a 39m thick unit of red-brown clay with sand. Then a 11m thick layer of alternating beds of red-brown clay with marl and silt is overlaying a 10m thick formation of gray-blue marls. Down to the depth of the deepest borehole station of 83.4m, an alternation of marly-sandy limestones and marls can be found which is underlain by blocks of cretaceous limestone representing the engineering bedrock at the site (Roumelioti *et al.* 2020). The general description of the soil column's lithostratigraphy at ARGONET vertical array is shown in Figure 5.

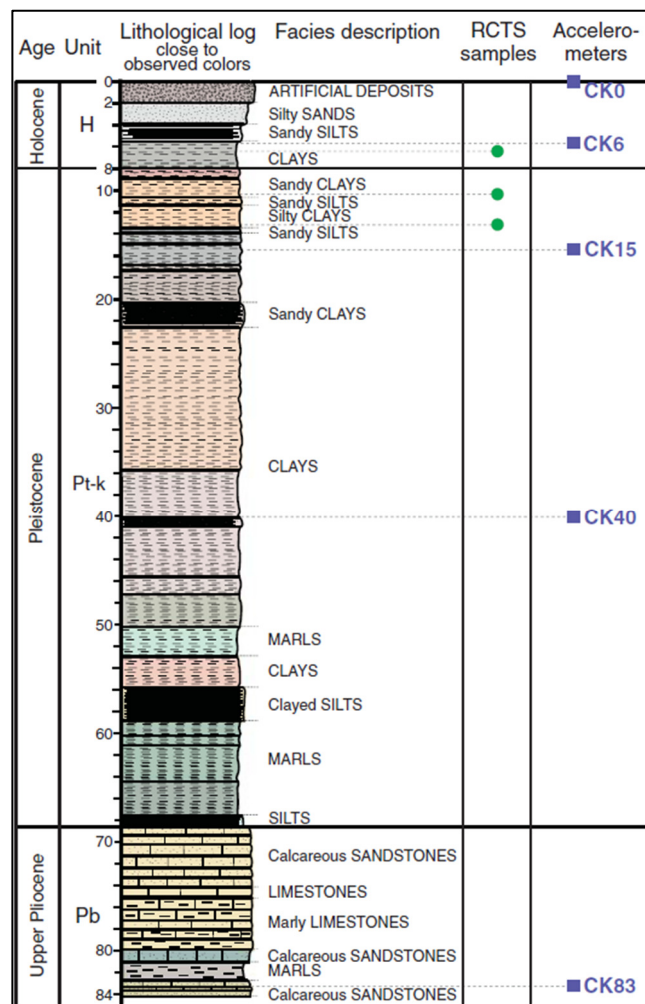


Figure 5. Lithologic description of facies with location of resonant column tests (RCTS) and accelerometers in the soil column at ARGONET vertical array. (Reproduced and modified from Theodoulidis *et al.* 2018).

1.2.3.2. Seasonal variation of shear wave velocity

The near-surface shear wave velocity V_S is a key parameter involved in many aspects of earthquake engineering as, e.g., soil liquefaction or earthquake ground-motion prediction. A correlation between V_S variation and seasonal weather variation i.e., varying soil moisture, has been intensively investigated within several research projects and demonstrated by laboratory experiments. Yeganeh and Fatahi (2018) showed that buildings experience different load under different moisture content of shallow soil during seismic events, and that extended dry periods may lead to greater earthquake ground motion impacts.

The study of Roumelioti *et al.* (2020) shows the possibility to trace the effect of weather seasons on V_S even at very shallow depth and at low-shaking levels based on earthquake records of the ARGONET array. Seismic interferometry effectively measures V_S by using vertical arrays and data gained from earthquakes or ambient vibrations of the ground. The method was applied to obtain the impulse response of medium between two receivers. Because ARGONET is a vertical array, V_S at different depth intervals could be computed.

Figure 6 c and d show variations of V_S between August 2015 and January 2018 retrieved for the depth intervals 0–5.6 m and 0–40.1 m, respectively. This variation is compared with rainfall (Figure 6 a) and corresponding water content (storage amount S) stored in the respective layers of soil.

Measurements reveal that the season-dependent cycling pattern of V_S is negatively correlated to precipitation data. Roumelioti *et al.* (2020) observed an abrupt fall in V_S immediately after heavy rainfall periods (marked by *blue* rectangles in Figure 6), following long dry periods in the studied area (marked by *red* rectangles in Figure 6). V_S values remain low compared to values of the dry period throughout the entire rainy season. A slower, gradual increase of V_S can be observed in spring reflecting the similarly slow process of soil drying. The identified pattern could be associated with changes in shallow moisture and corresponding changes in saturation S caused by rainfall infiltration.

It was estimated that the seasonal V_S variation could be as high as 40% of the yearly minimum by considering the existence of a shallow (2–3 m) aquifer at the study site. The shallow water table characterizing this site is not expected to fluctuate significantly due to

the proximity of the site to the coastline. Therefore, the V_S variation observed for depth 0–5.6 m is expected to be confined within the top 2m of soil.

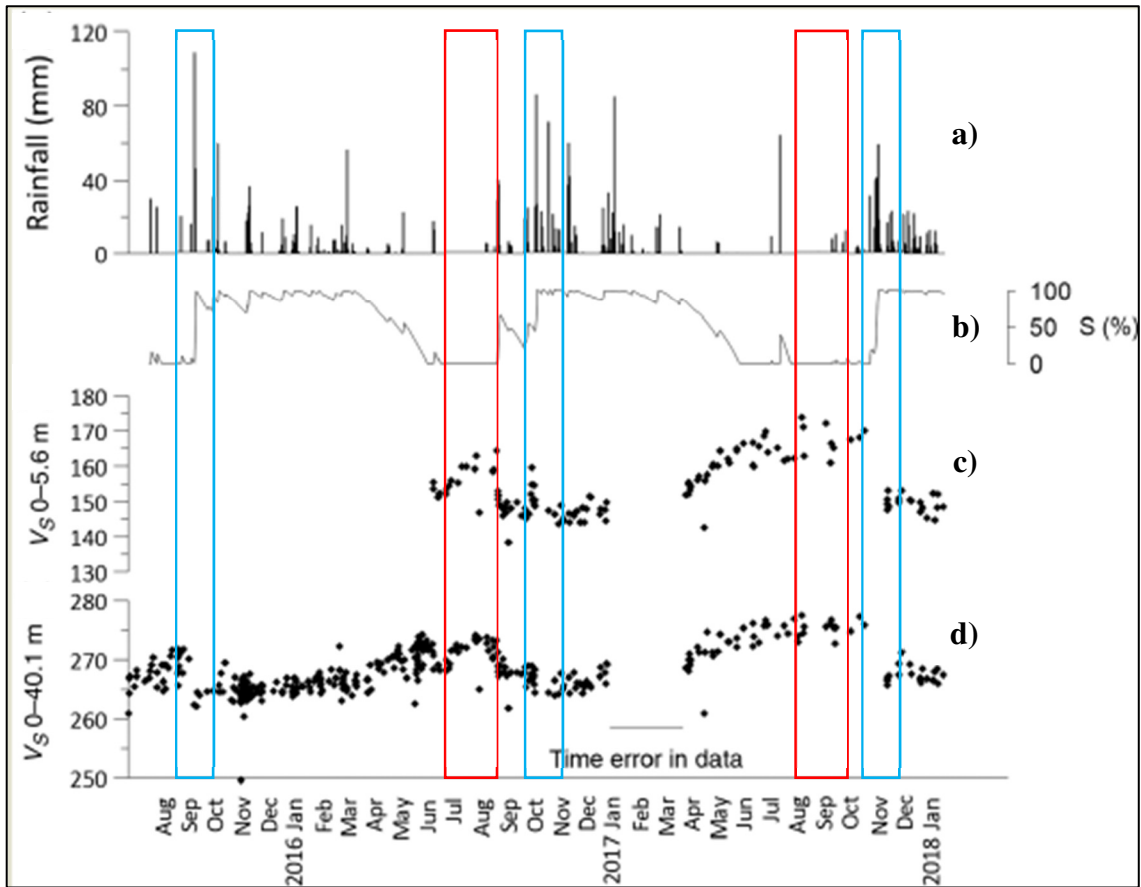


Figure 6. a) Rainfall amount and corresponding b) water storage amount S of the soil at ARGONET as proxy of soil moisture with interferometry based V_S - values for the depth ranges of c) 0-5.6 m and d) 0-40.1m showing the negative correlation between the season-dependent cycling pattern of V_S and precipitation data of the site. Blue marking periods of heavy rainfall, red marking periods of low rainfall. The graph reproduced from Roumelioti *et al.* (2020).

In addition to interferometry, the site's V_S profile was determined by inversion of the dispersion curves of Rayleigh surface waves. This analysis reveals the effect of the season on V_S as well. It leads to a significantly different value of V_S within the top 2m layer in the wet season, $V_S = 155 \text{ m/s}$ compared to the value found by Cushing *et al.* (2020) for the dry season, $V_S = 250 \text{ m/s}$. Therefore, results of surface wave dispersion analysis verify that V_S variations found by interferometry can be confined within the top 2m-layer. Results of dispersion analysis most likely correspond to the fundamental mode of Rayleigh waves and are presented in Figure 7.

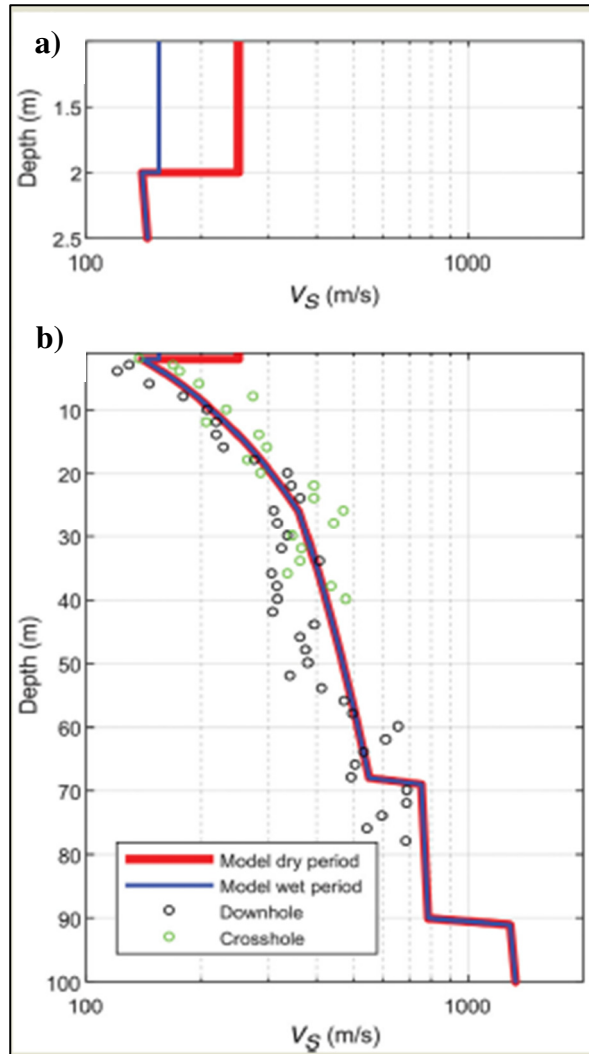


Figure 7. V_S - profile of the ARGONET site for the dry (*red*) and wet (*blue*) periods of the year down to **b)** 100 m and zoomed in to **a)** the first 2.5 m.

Black and *green* circles show results of downhole and crosshole measurements, respectively, used to build the dry model presented in Cushing *et al.* (2020).

By extending the analysis of interferometry to the vertical component of the ARGONET data, Roumelioti *et al.* (2020) showed that no variation of V_P could be reliably resolved due to small sampling rate. However, by upsampling the interferograms a V_P variation pattern resembling the variation of V_S for the 0–5.6 m depth interval could be obtained. Even though this is on the verge of resolution, it suggests that V_P is affected by the same process which is affecting V_S in the shallow soil.

2 Goals of the Thesis

The main goal of this thesis is to investigate the observed seasonal variation of the S-wave speed in the uppermost 2m-thick sedimentary layer in Argostoli, Cephalonia Island, Greece, due to rainfall-induced variation of water content in the layer.

We assume that the layer can be modelled as a poroelastic medium. Further we assume that the observed S-wave speed variations are due to rainfall-induced variations of the water content in pores.

Given the extremely limited input information, we have to address the following partial goals:

- a) develop a computational program with an implementation of the Neighbourhood Algorithm suggested by Sambridge *et al.* (1999a); the algorithm assumes known values of several elastic and/or poroelastic parameters and finds optimal values of the remaining (unknown) parameters,
- b) perform a parametric search of poroelastic models of the sedimentary layer in the dry season, that is, poroelastic air-saturated models,
- c) determine a physically acceptable model with the numerically most successful dry poroelastic models,
- d) search values of water saturation and values of matrix parameters for the found model with the S-wave speed value observed in the wet season,
- e) draw conclusions based on the entire procedure.

3 Development of a methodology for investigating effects of pore saturation on seismic wave speeds in the top 2m layer at the ARGONET vertical array

3.1. Estimation of poroelastic parameters

The estimation of poroelastic parameters of rocks in sedimentary structures and reservoirs is of great importance for quantifying the effect of porous fluid saturated rocks on seismic wave speeds and earthquake ground motion. To theoretically estimate poroelastic material parameters, inverse rock physics modelling techniques are used. These techniques link physical properties of rocks to geophysical and petrophysical observations. For the most recent development in rock physics modelling, the reader is referred to Das & Sengupta (2021) and Li *et al.* (2019) which present research results covering advanced applications on rock physics methods.

In Biot theory we can represent all fundamental poroelastic material parameters (1.11) as vector

$$\mathbf{m} = \{\rho_s, K_s, \rho_f, K_f, \eta, K_m, \mu_m, \phi, T, \kappa_0, n_J\} \quad (3.1)$$

In Biot-Gassmann theory, where an effective fluid phase is used, vector \mathbf{m} has the following form

$$\mathbf{m} = \{\rho_s, K_s, \rho_a, \rho_w, K_a, K_w, \eta_a, \eta_w, K_m, \mu_m, \phi, T, \kappa_0, n_J, e, S_a\} \quad (3.2)$$

In both theories, the vector of material parameters \mathbf{m} fully represents a poroelastic model.

In general, the vector of material parameters \mathbf{m} needs to be inverted from data defined as seismic parameters e.g., wave speeds, density, attenuation quality factors, electrical resistivity data or full-waveform data, which can be inferred from seismic records. In this thesis we restrict ourselves to seismic parameters, which were constrained by seismic observations at the study site in Argostoli, Greece (see section 1.2). Therefore, this data can be represented as the following vector

$$\mathbf{d} = \{V_P(f_r), V_S(f_r), Q_P(f_r), Q_S(f_r), \rho(f_r)\} \quad (3.3)$$

where V_P and V_S are fast P-wave and S-wave speeds, respectively, defined as VP_{fast} in Eq. (1.26) and VS in Eq. (1.28). Q_P and Q_S are quality factors of fast P-wave and S-wave, respectively. Their inverse values, describing attenuation due to friction between solid matrix and fluid in the pores, are defined as QP_{fast}^{-1} in Eq. (1.29) and QS^{-1} in Eq. (1.31). ρ is the average bulk density of the material (1.7).

Since seismic parameters are measured at some reference frequency f_r , we explicitly presented the dependency of parameters on this frequency in (3.3).

As far as we know, there are no field measurements of velocity and quality factor of the slow P-wave. Therefore, these parameters are not part of the vector \mathbf{d} .

As mentioned earlier, vector of material parameters \mathbf{m} can be obtained from vector of constrained data \mathbf{d} by inversion, while the inverse problem can be formulated as

$$\mathbf{m} = g^{-1}(\mathbf{d}) \quad (3.4)$$

where g is a nonlinear function and superscript $^{-1}$ refers to the inverse of this function. In our case, g represents a set of relations consisting of average bulk density (1.7) as well as dispersion and attenuation relations in (1.19) and (1.25)-(1.31). Therefore, to find vector \mathbf{m} we need to find the inverse of the nonlinear function g which is impossible in our case. However, finding g^{-1} can be circumvented by using an optimization method.

Generally, optimization methods search for the optimal solution over the whole model domain. These methods consist of exploring the whole model space (inverted parameters) only limited by minimum and maximum values.

In this thesis we use a search-based optimization method called Neighbourhood Algorithm (NA). The NA is not a global optimization method meaning that one single global optimal solution is not guaranteed. The NA based on the work of Sambridge (1999a) will be addressed in the next subsection. With the help of Dr. David Gregor, we developed a computational program with an implementation of the NA, which searches for optimal poroelastic parameters. The application of this program to data of the Argostoli site and corresponding results will be shown and discussed in chapter 4.

3.2. The Neighbourhood Algorithm

The NA is a direct search optimization method for searching models of acceptable data fit in a multidimensional parameter space. Generally, direct methods are derivative-free i.e., they do not use derivative information to find an optimal solution. Therefore, the NA belongs to the same class of methods as simulated annealing, genetic algorithm, and the uniform Monte Carlo method. All these methods use random distribution when exploring the parameter space.

As far as we know, the first application of the NA to geophysical problems was presented in the work of Sambridge (1999a). Sambridge's computational code containing the NA is freely available on <http://rses.anu.edu.au/~malcolm/na/> for registered users. It should be noted that the code can be used for different geophysical applications (e.g., see <http://rses.anu.edu.au/~malcolm/na/papers.html>).

The usage of the NA for inverse rock physics modelling was presented in Dupuy *et al.* (2016a) for the first time. After that many papers focusing on the same topic followed (Dupuy *et al.* 2017, Garambois *et al.* 2019, Yan *et al.* 2019, Dupuy *et al.* 2021a, Dupuy *et al.* 2021b). Orientated on Dupuy *et al.* (2016a), we used Sambridge's computational code in the same manner.

The NA uses uniform random distribution of points which drives the search for models. For each point of random distribution, a convex polygon, called a Voronoi cell, is constructed. Each Voronoi cell is defined by the position of its random point (also called nucleus), while any arbitrary picked point inside a given Voronoi cell is closer to its nucleus than to any other nucleus of a different cell. Therefore, Voronoi cells are sometimes denoted as nearest neighbour regions. Their mathematical definition can be formulated in the following way:

Let X be a d -dimensional metric space with L_2 norm $\|\cdot\|$ which characterizes the distance between any 2 points (nuclei). Let $P = \{m_1, \dots, m_N\}$ be a set of points (nuclei) in this d -dimensional space and let N be a whole number running from $2 \leq N < \infty$. Assuming $m_i \neq m_j$ for $i \neq j$, the Voronoi cell V of point (nuclei) m_i can be defined as

$$V(m_i) = \{x \in X \mid \|x - m_i\| \leq \|x - m_j\| \text{ for } i \neq j; (i, j = 1, \dots, N)\} \quad (3.5)$$

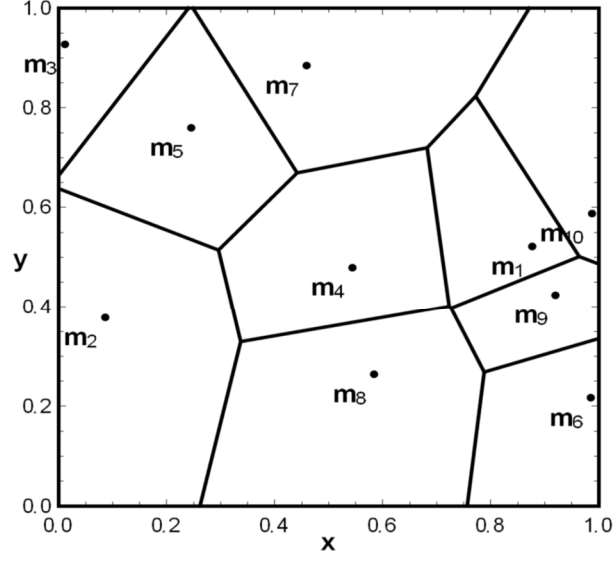


Figure 8. 2-dimensional bounded metric space partitioned by Voronoi cells.

It should be noted that in general m_i can be treated as vector with its number of components corresponding to the d -dimensionality of the metric space X . Therefore, from now on we will use bold font to represent the vector nature of m_i .

In Figure 8 we can see an example of a 2-dimensional space bounded in the x , y direction and partitioned by 10 Voronoi cells. Each Voronoi cell has its own nucleus corresponding to a two-component vector $m_i = \{x_i, y_i\}$, $i = 1, \dots, 10$.

In our case, the metric space is represented by a space containing poroelastic material parameters. We refer to this space as a parameter space, which is bounded by upper and lower limit values of poroelastic material parameters which are physically plausible. Any vector within this parameter space must have the number of components equal to the dimensionality of this space.

If we assume having a parameter space containing fundamental poroelastic material parameters according to Biot Theory, its dimensionality is 11, and all the vectors m_i , $i = 1, \dots, N$ within this space will have the following form

$$m_i = \{\rho_s, K_s, \rho_f, K_f, \eta, K_m, \mu_m, \phi, T, \kappa_0, n_J\}, i = 1, \dots, N \quad (3.6)$$

where N represents the total number of the vectors (and Voronoi cells).

Since we will be working with vectors \mathbf{m}_i , $i = 1, \dots, N$ containing only poroelastic material parameters, we can refer to these vectors as a model vectors, from which each of them can unambiguously represent a poroelastic material (poroelastic model).

The NA searches for an optimal solution iteratively. This means that in each iteration the parameter space is partitioned by a newly created set of Voronoi cells. Moreover, the denser the population of Voronoi cells in some regions of parameter space, the better the chance of having an optimal solution in those regions.

3.2.1. Limit values of parameter space

The parameter space needs to be bounded by lower and upper limit values. Since our parameter space contains poroelastic material parameters, we can identify the lower and upper limit values with physically plausible values corresponding to poroelastic sedimentary rocks.

Based on the available literature on numerical modelling in poroelastic materials, we present the lower and upper limit values of poroelastic parameters in Table 2. It should be noted that the represented bounds can be further refined if additional geological data of the site of interest are available.

Table 2. Lower and upper limit values of poroelastic material parameters corresponding to poroelastic sedimentary rocks.

Symbol	Units	Lower & Upper limit values
ρ_s	kg / m^3	2500–3000
K_s	GPa	1–50
ρ_f	kg / m^3	1–1100
K_f	GPa	$101 \cdot 10^{-6}$ – 2.6
K_m	GPa	0–50
μ_m	GPa	0–50
ϕ		0–0.5
T		1–3
κ_0	m^2	$10 \cdot 10^{-15}$ – $10 \cdot 10^{-8}$
n_J		1–10
S_a		0–1
e		1–40

3.2.2. Misfit function of seismic constrained and predicted data

The NA searches for an optimal solution by minimizing the misfit function χ^2 . In general, the misfit function describes the discrepancy between a priori known and theoretically predicted (synthetic) data corresponding to some model.

As we mentioned in section 3.1, we use as known data the seismic parameters constrained by observations at the site of interest. Recalling relation (3.3), the vector of seismic parameters \mathbf{d} at reference frequency f_r has the following form

$$\mathbf{d} = \{V_P(f_r), V_S(f_r), Q_P(f_r), Q_S(f_r), \rho(f_r)\} \quad (3.7)$$

It should be noted that not every time all the components of vector \mathbf{d} are known. As section 4.1 will show, sometimes only a limited number of constrained seismic parameters are available (e.g., only seismic velocities and density).

The theoretically predicted data are in general determined from the solution of a forward procedure. In our case the forward procedure is represented by velocity dispersion, quality factor and average bulk density relations in subsection 1.1.6. Using model vector \mathbf{m}_i corresponding to the i -th Voronoi cell, dispersion relations (1.19) and (1.25)-(1.28), quality factor relations (1.29)-(1.31), and density relation (1.7) we can calculate predicted seismic parameters at reference frequency f_r

$$V_P^{pred}(f_r), V_S^{pred}(f_r), Q_P^{pred}(f_r), Q_S^{pred}(f_r), \rho^{pred}(f_r) \quad (3.8)$$

These parameters are not measured, they are calculated using poroelastic material parameters in model vector \mathbf{m}_i .

Using data from (3.7) and (3.8) for model vector \mathbf{m}_i , we can define our misfit function in the following way

$$\begin{aligned} \chi^2(\mathbf{m}_i) = & \left(\frac{V_S(f_r) - V_S^{pred}(f_r, \mathbf{m}_i)}{V_S(f_r)} \right)^2 + \left(\frac{V_P(f_r) - V_P^{pred}(f_r, \mathbf{m}_i)}{V_P(f_r)} \right)^2 \\ & + \left(\frac{\rho(f_r) - \rho^{pred}(f_r, \mathbf{m}_i)}{\rho(f_r)} \right)^2 \\ & + \left(\frac{Q_S(f_r) - Q_S^{pred}(f_r, \mathbf{m}_i)}{Q_S(f_r)} \right)^2 + \left(\frac{Q_P(f_r) - Q_P^{pred}(f_r, \mathbf{m}_i)}{Q_P(f_r)} \right)^2 \end{aligned} \quad (3.9)$$

Looking at Eq. (3.9) we see that only predicted data depend on the model vector \mathbf{m}_i corresponding to i -th Voronoi cell. Moreover, it is assumed that $\chi^2(\mathbf{m}_i)$ is constant within the corresponding Voronoi cell.

In case of the NA, the process of minimizing the misfit function χ^2 in each iteration is carried out by creating a new set of Voronoi cells within the old cells with lower misfit relative to the rest of the cells. In best case scenario this should ensure an overall decrease of the misfit value with an increasing number of iterations.

In the next subsection we present the input parameters of the NA which control the creation of Voronoi cells and control the process of partitioning of the parameter space.

3.2.3. Control parameters

The main advantage of the NA is that it requires only a small number of control parameters. According to Sambridge (1999a) the NA even works with a minimum number of 2 control parameters. In this thesis, we work with 4 control parameters which allow us to have a better control over generating the model vectors (Voronoi cells). We denote these control parameters as n_{si} , n_r , n_s and N_{iter} .

The control parameter n_{si} represents the number of initial model vectors randomly generated before the first iteration. Graphically this corresponds to initially partitioning the parameter space into n_{si} Voronoi cells, while one nucleus of a Voronoi cell corresponds to one model vector.

The control parameter n_r represents the number of model vectors with the lowest misfit values at the current iteration. Graphically this corresponds to selecting the n_r Voronoi cells in the lowest misfit regions which can then be resampled into new Voronoi cells for the next iteration.

The control parameter n_s in the relation n_s / n_r represents the number of newly, randomly generated model vectors at the current iteration. Graphically this corresponds to creating n_s / n_r Voronoi cells inside each of the previously selected n_r Voronoi cells. This process is sometimes denoted as resampling process. It should be noted that n_s / n_r division with remainder does not pose a problem, since this results in assigning more newly created Voronoi cells to the top best models.

The control parameter N_{iter} represents the total number of iterations. If we denote it as a variable of current iteration, then it runs from $0, 1, \dots, N_{iter}$ and $it = 0$ corresponds to the moment when initial model vectors are created.

Additionally, we can introduce 2 auxiliary variables n and N . The parameter n denotes the number of most recently generated model vectors and parameter N denotes the total number of model vectors generated after it iterations.

The process of generating model vectors (Voronoi cells) in the NA, using the above-mentioned control and auxiliary parameters, is summarized in Figure 9.

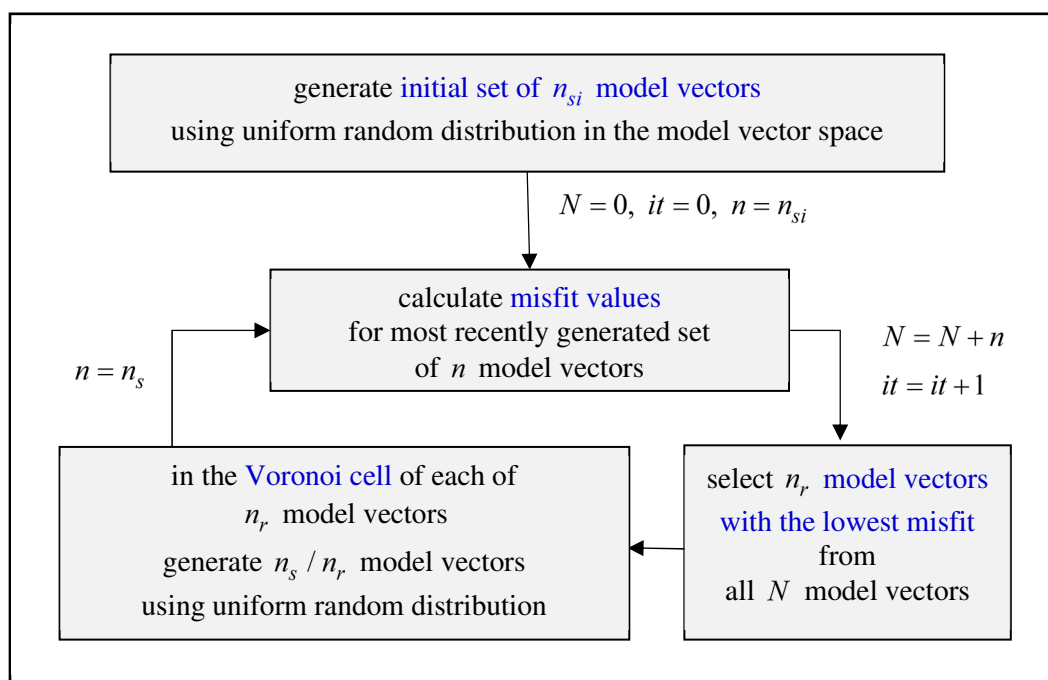


Figure 9. Scheme describing the procedure of the NA.

From Figure 9 we can clearly see that after a total of N_{iter} iterations, the number of model vectors is

$$n_{si} + n_s \cdot N_{iter} \quad (3.10)$$

Investigations of the misfit reduction with increasing number of iterations led to the conclusion of fixing the maximum number of iterations to $N_{iter} = 10000$ for receiving reasonable final lowest misfit models.

So far it was not mentioned how the random generation of model vectors is ensured in the NA. There are 2 options of randomly generating model vectors: In uniform pseudo-random (PR) manner or in uniform quasi-random (QR) manner. However, in this thesis we solely use uniform PR generation of model vectors.

3.2.4. Random number generation

As mentioned in the previous subsection, the method how model vectors are generated is purely random. More specially, the distribution of model vectors corresponds to the uniform pseudo-random (PR) sequence.

In our program the PR generation of model vectors in the NA is implemented through the computational routine *ran3*, which can be found in Press *et al.* (1993).

As most of the PR generators, also *ran3* must be initialized by an arbitrary integer number before being called. This initialization number is called random seed. A PR sequence is completely determined by the value of the random seed s . Thus, if a PR generator is reinitialized with the same seed value, it produces the same sequence of numbers (model vectors). If the PR generator is initialized with a different seed value, it produces a different sequence of model vectors.

Therefore, the sequence of initial model vectors is different for different random seed values which may result in significantly different values of poroelastic parameters found by the NA. The effect of using a set of randomly generated seed values for the inversion of poroelastic parameter values is described in chapter 4.

3.2.5. Visualization of the search for an optimal solution in the parameter space using the NA

Here we present a simple example of the search for an optimal solution (model vector with lowest misfit value) in a 2-dimensional parameter space using the NA. We also try to show the role of control parameters, presented in subsection 3.2.3, through the visualization of this search. Due to simplicity and as an example, only the first iteration of the NA is shown.

In Figure 10 we see 6 frames denoted by letter $a) - f)$ which all represent the same 2-dimensional space bounded in the x, y direction. Axes x and y may represent physical material parameters bounded by upper and lower limit values, in this case 0 and 1, respectively.

For this simple example we assume the following controlling parameters

$$\begin{aligned}n_{si} &= 10 \\n_s &= 10 \\n_r &= 2\end{aligned}\tag{3.11}$$

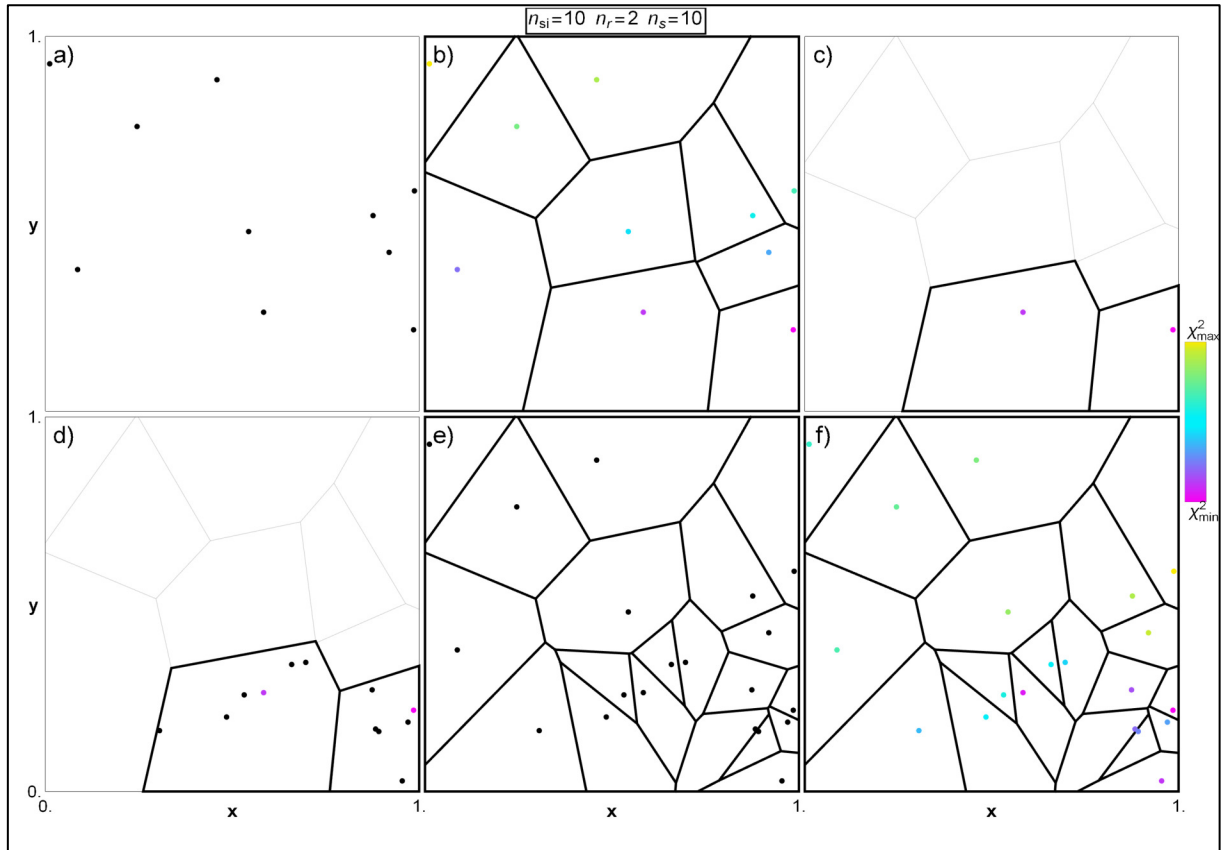


Figure 10. Visualization of the search for a model vector in a 2-dimensional parameter space using the NA.

In frame *a)* of Figure 10 the $n_{si} = 10$ initial 2-dimensional model vectors are PR generated in the parameter space and indicated by black points. This corresponds to iteration $it = 0$ of the NA.

As mentioned in section 3.2, each Voronoi cell has its own nucleus which can be associated with one model vector. By doing that at $it = 1$, the parameter space in Figure 10 *b)* is partitioned into 10 Voronoi cells. In addition, the misfit function for each of the model vectors must be calculated. The value of the misfit function χ^2 for each model vector can be visualized by assigning a color to each nucleus (point) according to the color scheme running from χ^2_{\min} to χ^2_{\max} and pictured on the right side of the frames in Figure 10.

Since we chose $n_r = 2$, the two Voronoi cells with lowest misfit values are selected. They are highlighted in black color in Figure 10 *c)*. As mentioned earlier, the misfit value is constant within each Voronoi cell.

In frame *d)* of Figure 10 the $n_s/n_r=10/2=5$ new model vectors are randomly generated inside each of the two selected Voronoi cells. The new model vectors are indicated by points in black color. The generation of new model vectors in these Voronoi cells is natural since we aim to sample the areas with the lowest misfit values.

After generating new model vectors, a new partitioning of the parameter space by Voronoi cells needs to be recalculated. This new partitioning is pictured Figure 10*e)*. We can see that the area of the lowest misfit is sampled more densely compared to the rest of the parameter space. This means that the search for an optimal solution is attracted to the low misfit areas.

In the Figure 10*f)* the misfit values for 10 new model vectors is calculated and a color to each nucleus as in Figure 10*b)* is assigned. One can see that after the first iteration there is a total number of $N=10+10=20$ models.

The search process for an optimal solution depicted in Figure 10*b)–f)* is then repeated for the next iteration $it=2$ followed by the rest of all iterations.

3.3. Terminology of parameters in our study

Throughout the work presented in this thesis we developed a computational program with an implementation of the NA to search for optimal poroelastic parameters describing the material at the site in Argostoli, Greece (see section 1.2). Based on limited input information of seismic parameters of wave speeds and density, constrained by observations, we performed inversions for both, dry and wet, seasons denoted as “wet” and “dry”, respectively. Corresponding parameters for both seasons used in the sections of chapter 4 are defined as the following.

Seismic parameters: Parameters constrained by seismic observations in the dry season

$$\{V_P^{dry}, V_S^{dry}, Q_P^{dry}, Q_S^{dry}, \rho^{dry}\} \quad (3.12)$$

or wet season

$$\{V_P^{wet}, V_S^{wet}, Q_P^{wet}, Q_S^{wet}, \rho^{wet}\} \quad (3.13)$$

Table 3. Seismic parameters constrained by observations.

Symbol	Name	Units
V_S	S-wave speed	m / s
V_P	P-wave speed	m / s
ρ	average bulk density	kg / m^3
Q_S	S-wave quality factor	
Q_P	P-wave quality factor	

Poroelastic parameters: Fundamental poroelastic material parameters describing a poroelastic model in Biot theory

$$\{\rho_s, K_s, \rho_f, K_f, \eta, K_m, \mu_m, \phi, T, \kappa_0, n_J\} \quad (3.14)$$

and in Biot-Gassmann theory

$$\{\rho_s, K_s, \rho_a, \rho_w, K_a, K_w, \eta_a, \eta_w, K_m, \mu_m, \phi, T, \kappa_0, n_J, e, S_a\} \quad (3.15)$$

Table 4. Poroelastic parameters describing a poroelastic model.

Symbol	Name	Units
solid phase		
ρ_s	density	kg / m^3
K_s	bulk modulus	Pa
effective fluid phase		
ρ_f	density	kg / m^3
K_f	bulk modulus	Pa
η	dynamic viscosity	$Pa s$
S_a	air saturation	
e	Brie exponent	
solid matrix (drained)		
K_m	bulk modulus	Pa
μ_m	shear modulus	Pa
ϕ	porosity	
T	tortuosity	
κ_0	permeability	m^2
n_J	dimensionless parameter	

Predicted parameters: Parameters calculated using poroelastic parameters in relations (1.19), (1.25)-(1.31), and (1.7)

$$\{VS^{pred}, VP_{fast}^{pred}, VP_{slow}^{pred}, \rho^{pred}, QS^{pred}, QP_{fast}^{pred}, QP_{slow}^{pred}\} \quad (3.16)$$

Table 5. Predicted parameters of the inversion calculated using poroelastic parameters.

Symbol	Name	Units
VS	S-wave speed	m / s
VP_{fast}	fast P-wave speed	m / s
VP_{slow}	slow P-wave speed	m / s
ρ	average bulk density	kg / m^3
QS	S-wave quality factor	
QP_{fast}	fast P-wave quality factor	
QP_{slow}	slow P-wave quality factor	

Control parameters of the NA: Computational parameters controlling the inversion

$$\{n_{si}, n_s, n_r, N_{iter}\} \quad (3.17)$$

Table 6. Control parameters of the inversion.

Symbol	Name	Value
n_{si}	the number of initially generated models	1000
n_s	the number of models generated in each iteration	10
n_r	the number of the resampled models	2
N_{iter}	the number of iterations	10000

4 Poroelastic models of the top 2m layer

4.1. Determination of seismic parameters for dry and wet seasons

Here we describe how we determined the values of seismic input parameters. We recall that the input parameters enter the inversion as data vector \mathbf{d} (3.7). All values discussed later correspond to the upper 2m thick layer at the ARGONET vertical array.

We use $V_S(f_r)$ obtained by inversion of dispersion curves of Rayleigh waves by Cushing *et al.* (2020) for dry season and Roumelioti *et al.* (2020) for wet season (see subsection 1.2.3). $V_S(f_r)$ is the only parameter determined by inversion of seismic observations. However, to better constrain the inversion of poroelastic parameters, we need as many input parameters as possible. Therefore, we also consider $V_P(f_r)$ estimated by Dr. Fabrice Hollender for the dry season. Additionally, we use empirical regression formulas by Brocher *et al.* (2005), to estimate the value of $V_P(f_r)$ for the dry season

$$V_P(f_r) = 0.9409 + 2.0947 \cdot V_S(f_r) - 0.8206 \cdot [V_S(f_r)]^2 + 0.2683 \cdot [V_S(f_r)]^3 - 0.0251 \cdot [V_S(f_r)]^4 \quad (4.1)$$

and values of $\rho(f_r)$ for both seasons

$$\rho(f_r) = \left(1.6612 \cdot [V_P(f_r)] + 0.4721 \cdot [V_P(f_r)]^2 + 0.0671 \cdot [V_P(f_r)]^3 - 0.0043 \cdot [V_P(f_r)]^4 + 0.000106 \cdot [V_P(f_r)]^5 \right) \cdot 1000 \quad (4.2)$$

Quality factor values estimated by the poroelastic inversion are values characterizing attenuation due to poroelastic effects i.e., dissipation of energy in the matrix-fluid interactions. This attenuation of seismic waves due to fluid friction was not constrained by seismic observations. Therefore, values of $Q_S(f_r)$ and $Q_P(f_r)$ remain unknown.

The parameters which are directly constrained by observations of seismic records are summarized in Table 7. The exact values of indirectly constrained parameters estimated by Brocher's formulas (Eqs. (4.1) and (4.2)) will be presented in the corresponding sections of inversions for dry and wet seasons.

A poroelastic medium is dispersive. Therefore, we explicitly associate a frequency with the seismic wave speeds, as explained in section 3.1. We consider three frequencies covering a broad frequency range: 20Hz , 100Hz and 10^8Hz . The first choice, 20Hz , relates to the frequency for which we assume the wave speed variations between seasons were observed (described in subsection 1.2.3). The second choice, 100Hz , presents an artificial choice to test the sensitivity of results of the inversion. The last choice represents an approximation of the infinite frequency. By considering three frequencies, we want to investigate and quantify the dependence of poroelastic output parameters on the frequency.

Table 7. Seismic parameters of the upper 2m-thick layer during dry and wet seasons directly and indirectly constrained by observations of seismic records.

Symbol	Units	Dry season	Wet season
$V_S^{obs}(f_r)$	m/s	250	155
$V_P^{obs}(f_r)$	m/s	600	estimated by Brocher's formula
$\rho^{obs}(f_r)$	kg/m^3	estimated by Brocher's formula	estimated by Brocher's formula

The exact sets of input parameters for the inversion, which are combining the seismic data vector parameters and other a priori known parameters, are presented in the following sections. The application of the inversion algorithm to seismic parameters obtained during the dry and wet seasons will be denoted as “dry inversion” and “wet inversion”, respectively.

4.2. Poroelastic Inversion for the dry season

4.2.1. Choices of input parameter sets

We investigate the sensitivity of poroelastic output parameters of the dry inversion considering 7 sets of input parameter values (see Table 8).

Because we do not have a direct estimation of bound water content of the unconfined 2m aquifer during dry season measurements, we assume for simplicity that the pore space is fully saturated by air (i.e., $S = S_a = 100\%$). Consequently, we consider fluid parameter values of air $\{\eta_a, K_a, \rho_a\}$ that can easily be found in literature (e.g., Lo & Sposio 2004) as commonly accepted values. Moreover, we assume $n_J = 8$, the value utilized in different applications by numerous authors (see subsection 1.1.2) because it can conveniently be used for various materials including unconsolidated sediments and clean sandstones.

Table 8. Choices (denoted as ‘‘C’’) of input parameter sets for the inversion of poroelastic parameters.

Red background indicates directly and indirectly constrained input parameters,
grey background indicates unknown parameters.

Symbol	Units	Values						
		C1	C2	C3	C4	C5	C6	C7
V_S^{dry}	m/s	250		250	250	250	250	250
V_P^{dry}	m/s		600	600	1417.38	600	1417.38	600
ρ^{dry}	kg/m^3					840.71	1580.44	1580.44
η_a	$Pa\ s$	$1.8 \cdot 10^{-5}$						
K_a	GPa	$0.145 \cdot 10^{-3}$						
ρ_a	kg/m^3	1.1						
n_J	$Pa\ s$	8						
f_r	Hz	$\{10^8, 10^2, 20\}$						

For C1 and C2, we only use one of the seismic wave speed values presented in Table 7. Although we expect the inversion to be insufficiently constrained by just one seismic input parameter value, we want to see if we are still able to obtain reasonable results.

For C3, we use both seismic wave speed values combined.

For C4 and C6, we estimate the P-wave speed using Brocher's formula (4.1). Although the resulting value is considered too high by Dr. Hollender, we include it in our tests as an endmember to investigate the sensitivity of poroelastic output parameters of the dry inversion. Density of C6 is estimated by Brocher's formula (4.2). We note that Brocher's formula can be applied for $V_p > 1500\text{m/s}$. However, the resulting value of density for $V_p = 1417\text{m/s}$ is reasonable.

For C5, we estimate the density using Brocher's formula (4.2). We use Brocher's formula outside of the designated range of P-wave speeds to see whether a reasonable density can still be obtained. We compare this resulting density with the minimum reasonable density of a poroelastic material of the top 2m layer at the site based on values reported in literature. For this, we consider an average solid grain density $\rho_s = 2650\text{kg/m}^3$ of coarse sand (Turgut & Yamamoto 1988) and lightly consolidated sand (Masson and Pride 2006). For porosity, we use $\phi = 0.5$ corresponding to the upper limit of values prescribed for the inversion (see Table 2). By using Eq. (1.7) we get a resulting average bulk density of $\rho = 1330\text{kg/m}^3$. Since the density estimated by Brocher's formula is smaller than this minimum plausible density value, we do not consider this choice in further tests.

For C7, we assume both wave speed values plus the same density value as in C6.

We performed preliminary inversions for C1 – C4 and C6 – C7. As we intuitively anticipated, inversion for C1 and C2 (with just one input parameter) and C3 and C4 (with two input parameters) were insufficiently constrained and did not lead to reasonable results. For C1, the inverted poroelastic parameters led to a P-wave speed value of $\sim 2400\text{m/s}$, which is unrealistically high for soft or unconsolidated sediments. Similar observations could be made for C2 – C4.

Therefore, we decided to consider only choices C6 – C7 with three seismic input parameters for further dry inversions. These choices led to acceptable values of the inverted poroelastic parameters and corresponding wave speeds.

It was not obvious a priori, what will be the scatter of values of the inverted poroelastic parameters for the three considered reference frequencies. We performed inversions for several randomly selected seed values. In all cases the inverted poroelastic parameters were close to each other for all three considered frequencies. We illustrate this in Table 9 for a selected seed value $s = 100$.

Table 9. Values of poroelastic parameters obtained for dry season for 2 input model choices (C6 and C7) and selected seed value $s = 100$.

Symbol	Units	Values					
		C6			C7		
		20Hz	10^2 Hz	10^8 Hz	20Hz	10^2 Hz	10^8 Hz
ρ_s	kg / m^3	2635.8	2635.8	2636.1	2636.02	2637.05	2635.45
K_s	GPa	39.95	39.95	39.97	34.85	35.08	34.89
K_m	GPa	3.04	3.04	3.04	0.437	0.438	0.437
μ_m	GPa	0.0988	0.0988	0.0988	0.0989	0.0989	0.0989
ϕ		0.401	0.401	0.401	0.400	0.400	0.400
T		2.850	2.850	2.857	2.827	2.767	2.792
κ_0	m^2	$1.1 \cdot 10^{-1}$	$1.1 \cdot 10^{-11}$	$1.3 \cdot 10^{-11}$	$7.2 \cdot 10^{-9}$	$7.7 \cdot 10^{-9}$	$7.8 \cdot 10^{-9}$

Using Eqs. (1.26) - (1.28) and (1.7), we calculate wave speeds, quality factors and density corresponding to inverted poroelastic parameters and using Eq. (3.9) we calculate the resulting misfit χ^2 and minimum misfit χ_{\min}^2 throughout all iterations. The results for C6 and C7 and for the three considered frequencies are summarized in Table 10. We note that only values with red colored rows contribute to the misfit function, since the remaining seismic parameters are not a priori known.

For both input model choices, C6 and C7, we see that obtained poroelastic parameter values (Table 9) and predicted values of VS , VP_{fast} and ρ (Table 10) do not significantly differ for different values of f_r . This is what we expected to see since the inversion searches for poroelastic parameters which lead to predicted wave speed and density values as close to the seismic input values as possible. Values of quality factors and slow P-wave speed are not constrained by the inversion but estimated as functions of frequency. Since the slow P-wave is the most dispersive wave and strongly dependent on frequency, it is good to see that the value varies for different values of f_r . Although attenuation due to poroelastic effects, i.e., fluid friction, is expected to result in big quality factor values since only a small amount of energy can be dissipated from the solid matrix into air, the values seem too large.

Table 10. Summary of seismic parameters calculated from inverted poroelastic parameter values for C6 and C7 (Table 9). *Red* background indicates parameters that contribute to the misfit function, whereas *grey* background indicates parameters that were not prescribed (see Table 8).

Symbols	Units	Values					
		C6			C7		
		20Hz	10^2 Hz	10^8 Hz	20Hz	10^2 Hz	10^8 Hz
VS^{pred}	m / s	250.00	250.00	250.00	249.99	250.00	249.95
VP_{fast}^{pred}	m / s	1417.38	1417.38	1417.38	600.01	600.01	599.99
VP_{slow}^{pred}	m / s	7.51	16.78	214.79	157.58	212.28	217.23
ρ^{pred}	kg / m^3	1580.44	1580.44	1580.44	1582.36	1582.69	1582.50
QS^{pred}		$2 \cdot 10^7$	$3 \cdot 10^6$	$4 \cdot 10^7$	$3 \cdot 10^4$	$3 \cdot 10^4$	$2 \cdot 10^{10}$
QP_{fast}^{pred}		$2 \cdot 10^7$	$5 \cdot 10^6$	$5 \cdot 10^7$	$3 \cdot 10^6$	$2 \cdot 10^6$	$2 \cdot 10^{12}$
QP_{slow}^{pred}		0.199	0.997	$1 \cdot 10^6$	$5 \cdot 10^4$	$23 \cdot 10^4$	$2 \cdot 10^{11}$
χ_{min}^2		$2 \cdot 10^{-17}$	$2 \cdot 10^{-16}$	$2 \cdot 10^{-16}$	$1 \cdot 10^{-6}$	$2 \cdot 10^{-6}$	$2 \cdot 10^{-6}$

Considering that the analysis of seismic records was performed for frequencies close to $f_r = 20Hz$, we will show further results only for $f_r = 20Hz$.

Comparing output poroelastic parameter values of both choices in Table 9, it is interesting to observe that the set of values of C6 gives relatively similar results as the set of C7, although both choices differ significantly in their prescribed P-wave speed values. All parameter values of ρ_s, μ_m, ϕ, T and κ_0 differ only by $< 0.1\%$ between C6 and C7. K_s of C7 is by 13% smaller than K_s of C6, while both values are in a reasonable range of solid grain density. K_m is the crucial parameter for determining V_p . Therefore, it is good to see that this is the parameter with most significantly different values of both choices found by the algorithm. K_m of C7 is only 15% of the C6 value. K_m for C6 is close to values found for materials as e.g., quartz or various sandstone types with significant clay content (Cheng 2016), whereas K_m of C7 can be found for lightly consolidated sand (Masson & Pride 2006). Since geological and geotechnical observations at the investigated site indicate that the 2m soil layer consists of artificial deposits (sandy and silty gravel), the value of matrix bulk modulus estimated by the C7 inversion is expected to be closer to

material values at the site. Therefore, we consider C7 as more reasonable input value set for the dry inversion, and we will show further results only for this choice.

In Figure 11, 2D sections of the parameter space (K_s versus ρ_s , μ_m versus K_m , T versus ϕ , κ_0 versus ϕ , χ_{\min}^2 versus it) are presented for the inversion of C7 with $f_r = 20\text{Hz}$ and $s = 100$. Each plot shows the values of inverted poroelastic parameters in the parameter space. The first $n_{si} = 1000$ randomly generated models are represented by grey colored points. The colors of the remaining models refer to the corresponding misfit value. Thus, the misfit function for pairs of inverted parameters can be analyzed and interpreted. The model with lowest misfit of the dry inversion is represented by a black cross.

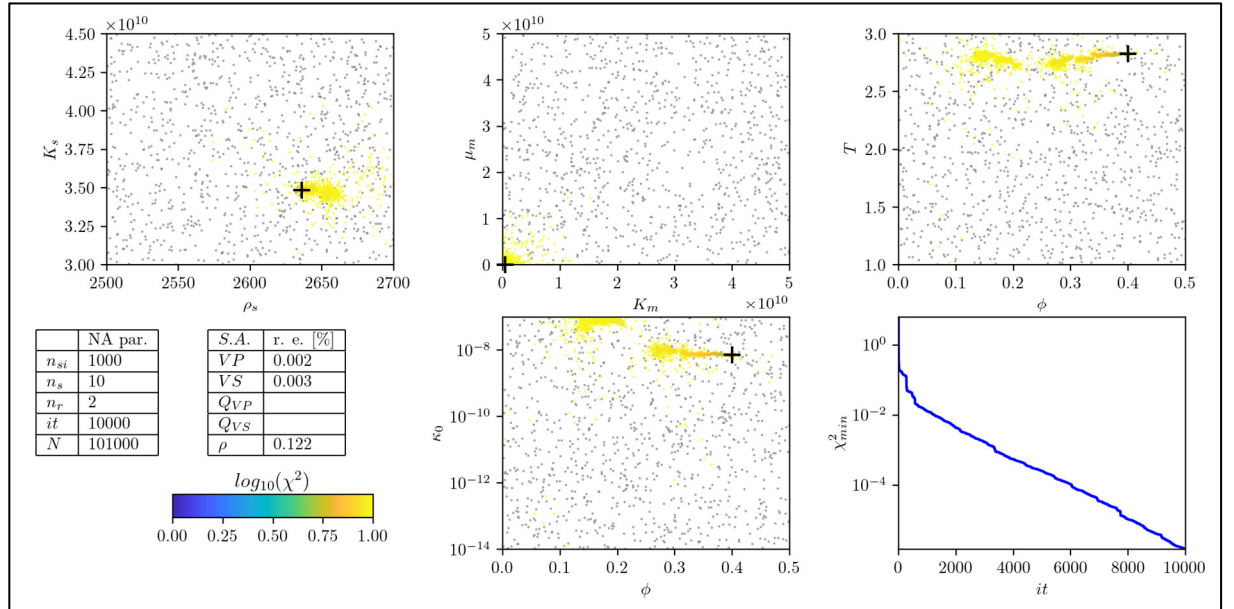


Figure 11. Inversion of poroelastic parameters for C7 with $f_r = 20\text{Hz}$ and $s = 100$.

Plots show the values of inverted models in the parameter space. Ranges of the axes are set by lower and upper limits of parameters defined within the inversion algorithm (Table 2).

Black crosses indicate model with the lowest misfit. *Grey* points indicate randomly generated models during the first iteration. Color of each remaining point depends on the misfit value of the corresponding model.

The bottom right plot shows the minimum misfit throughout all iterations.

For all parameter plots, only the more lightly colored models which correspond to relatively large misfit values are visible. Dark colored models which refer to lower misfit values are concentrated in a small spot covered by the black cross. This high concentration of lower misfit points indicates that models converge fast to the model of lowest misfit.

For bulk modulus and density of the solid (K_s and ρ_s) we see a high concentration of points near one local minimum, although the whole model space is investigated. Both parameters can be considered as well estimated. A similar conclusion can be obtained for matrix parameters (μ_m and K_m), which also converge to one local minimum of the observed model space. Tortuosity also has a clear minimum in the misfit function, whereas porosity values are more widely spread over the value range which can be observed in the top right 2D section. Similar results are obtained in the bottom middle 2D section of permeability and porosity.

In all cases, the dark colored points implying low misfit values are concentrated in one local minimum, which indicates an overall good estimation of all poroelastic parameters by the inversion. This is emphasized by the relative error values between seismic input and predicted parameter values for the model with lowest misfit, presented in the inset table in Figure 11. For density and both wave speeds, the relative error values are $< 1\%$, which is also indicated by the corresponding low misfit value of $\chi_{\min}^2 = 1 \cdot 10^{-6}$ (Table 10). Overall, the inversion based on the input parameter set of C7 leads to a considerably good estimation of poroelastic and predicted parameters. Therefore, C7 will be used for all further dry inversions.

4.2.2. Determination of models

The goal of the dry inversion is to obtain one final model of poroelastic parameter values representing the material of the upper 2m thick layer during the dry season. So far, we selected C7 as most convincing set of input parameter values. At the same time, we know that poroelastic output parameter values vary with varying random seed value (see subsection 3.2.4). Therefore, we will run the dry inversion for numerous randomly selected seed values. Based on different inversions on poroelastic parameters, we will then determine one final poroelastic model. This further procedure can be summarized with the following steps based on C7 at $f_r = 20\text{Hz}$:

- 1) Run the dry inversion for a set of randomly selected seed values.
- 2) Consider only the model with the lowest misfit for each inversion (i.e., for each considered seed value).
- 3) Select physically plausible models which fall into admissible ranges of predicted parameters, VP_{slow} and QP_{slow} .
- 4) Determine the final model with mean values of all poroelastic parameters (denoted as “mean value model”).

We run the dry inversion for 300 randomly selected seed values s . For each inversion corresponding to one seed value, we consider only the model of lowest misfit. This leads to 300 models. In Figure 12, 2D sections of the parameter space (K_s versus ρ_s , μ_m versus K_m , T versus ϕ , κ_0 versus ϕ , χ_{\min}^2 versus s) show the inverted poroelastic parameter values for each model. The color of each model refers to its misfit value. Thus, different poroelastic parameters of all models can be compared based on the scatter of points, while individual models can be compared based on their misfit value.

The parameters with the narrowest scatter of obtained values are matrix parameters (μ_m, K_m). All models are concentrated in one spot (see the top middle panel of Figure 12). This implies that the matrix parameters are independent on the seed value and thus can be considered as well resolved by the inversion. At the same time, we note that the values of $\mu_m = 0.099\text{GPa}$ and $K_m = 0.44\text{GPa}$ are close to the lower limit of 0GPa , defined for the inversion (Table 2). By running various inversions with different prescribed ranges of both matrix parameter values we investigated if changing the upper and lower limit values will affect the location of points. Since we always obtained the same values for both parameters, we can conclude that results of the inversion are not biased by prescribed ranges.

Another parameter with narrow scatter is porosity. All models are concentrated between 0.37-0.41 (see the T versus ϕ or κ_0 versus ϕ in Figure 12). ϕ depends on fluid, bulk, and solid densities (1.7). Therefore, the narrow scatter is likely related to the fact that the inversion includes a priori known fluid and bulk densities, and a relatively narrow range for solid density. This leads to an overall small range of possible porosity values.

The remaining parameters (K_s , ρ_s , κ and T) show a wide scatter and vary randomly within their prescribed ranges. There is no clear indication of a grouping of models with globally lower misfit. All models have a very small relative error of $< \pm 1\%$ between constrained and predicted parameter values indicated by very low misfits. Consequently, we can conclude that all models fit observations equally well. Therefore, we need additional criteria to select better models from worse ones.

To exclude unrealistic models and only keep physically plausible ones, we now select those which fall into admissible ranges of specific predicted parameters.

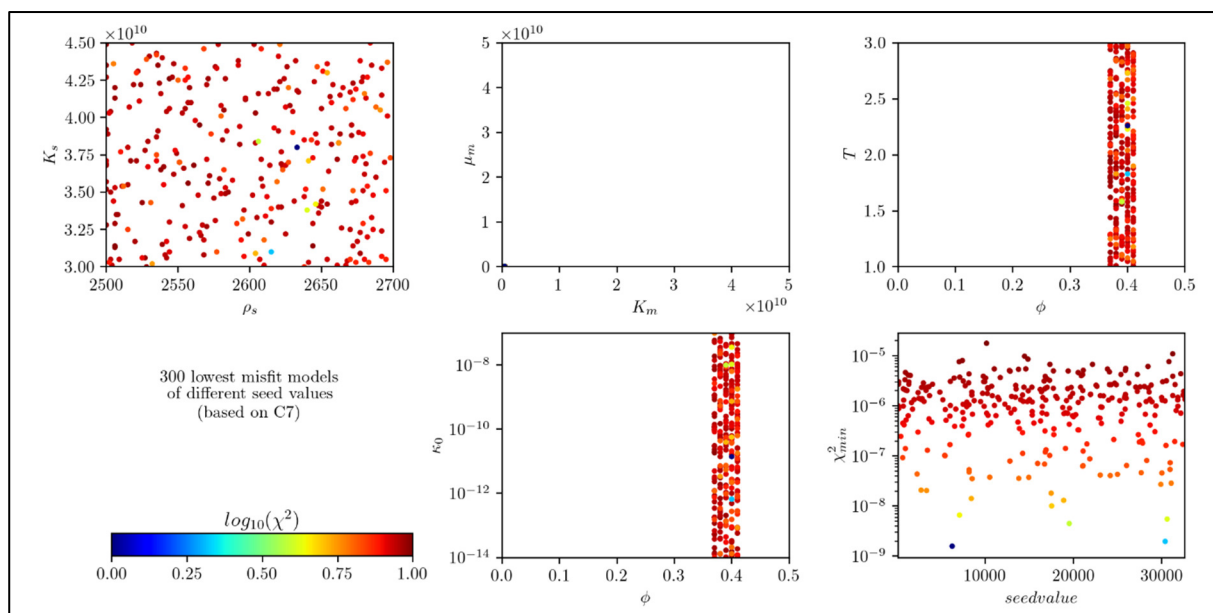


Figure 12. Lowest misfit models of 300 dry inversions corresponding to 300 randomly selected seed values. Plots show the parameter values of each model in the parameter space. Ranges of the axes are set by lower and upper limits of parameters defined within the inversion algorithm (Table 2). Color of each model depends on the corresponding misfit value. The bottom right plot shows the relation between misfit and seed value.

The slow P-wave usually behaves as a diffusive type of wave at low frequencies like 20Hz. This is due to its comparatively low phase velocity, high attenuation, and strong dispersion (see subsection 1.1.5). Figure 13 shows histograms of wave speed and quality factor for slow P-waves calculated for 57 models (sets of poroelastic parameter values)

based on available literature on poroelastic modelling (e.g., Dai *et al.* 1995, Picotti *et al.* 2007, Carcione *et al.* 2010). As the figure reveals, 50 models lead to $QP_{slow} < 0.02$ and $VP_{slow} < 100 \text{ m/s}$.

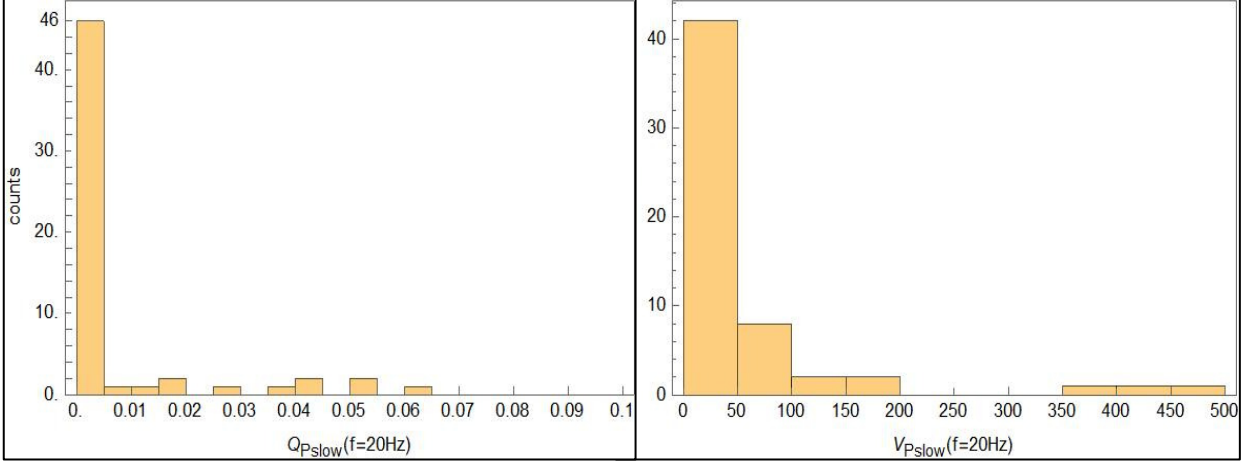


Figure 13. 57 values of QP_{slow} and VP_{slow} at 20Hz based on available literature of poroelastic modelling.

The left-side plot of Figure 14 presents predicted VP_{slow} and QP_{slow} values for all models of our dry inversion. We see that most models lead to high wave speed and quality factor values compared to those reported in literature (see Figure 13). To eliminate models with too high VP_{slow} and/or QP_{slow} , we decided to include two physical constraints:

$$QP_{slow} < 0.1 \quad (4.3)$$

$$VP_{slow} < 100 \text{ m/s} \quad (4.4)$$

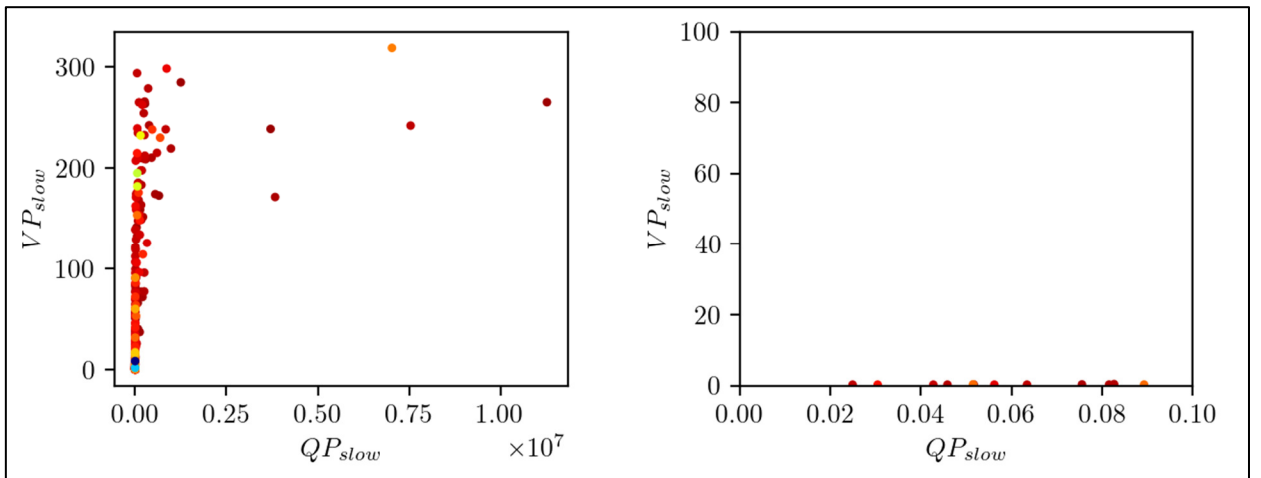


Figure 14. Scatter of QP_{slow} and VP_{slow} values of all 300 inverted models (*left*).

12 models which satisfy the conditions set by the physical constraints (4.3) and (4.4) (*right*).

Looking at the restricted models in the right-side plot of Figure 14 we see that that low QP_{slow} values automatically lead to low VP_{slow} values. Therefore, as intuitively anticipated, both conditions are correlated to each other and fulfilled at the same time.

Figure 15 presents similar 2D sections of the parameter space as Figure 12. Now just those models which fall into ranges defined by the criteria (4.3) and (4.4) are shown. There are 12 models out of 300 which satisfy our conditions set by the physical constraints.

The two bottom plots indicate that QP_{slow} and VP_{slow} are correlated with κ . The constraints lead to an exclusion of models representing high permeable sediments. The 12 remaining models have low permeability values of $\kappa < 10^{-13}$. Although the new parameter bounds of QP_{slow} and VP_{slow} eliminate higher permeable sediments, the results are consistent with models used by most authors (Figure 13). Furthermore, such comparatively low values of permeability in the range of $10^{-12} - 10^{-16} m^2$ can often be found for sandy clays like quartz but also different types of sandstones (Cheng 2016), which are both possible constituents of the material composition at the site. Therefore, it is reasonable to constrain the models by the physical conditions for VP_{slow} and QP_{slow} and consequently represent low- or moderate permeable sediments.

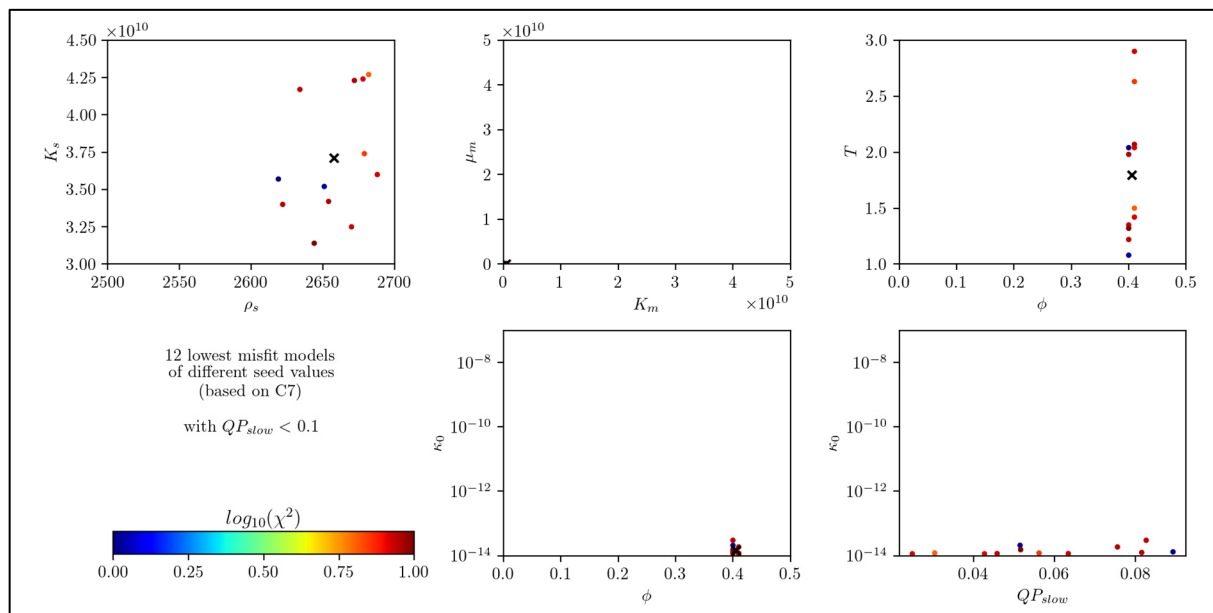


Figure 15. 12 models with $QP_{slow} < 0.1$ and the mean value model indicated by a black cross.

Plots show the parameter values of each model in the parameter space. Ranges of the axes are set by lower and upper limits of parameters defined within the inversion algorithm (Table 2). Color of each model depends on the corresponding misfit value. The bottom right plot shows the correlation between permeability and slow P-wave speed.

Given limited information about material composition of the top 2m layer at the site, further physical restrictions on material parameter values are difficult to make. Therefore, we represent the 12 models by mean values of all poroelastic parameter values. The mean values are summarized in Table 11 and indicated by black crosses in Figure 15.

Table 11. Mean value model of dry inversion.

Symbols	Units	Values
ρ_s	kg / m^3	2657.8
K_s	GPa	37.13
K_m	GPa	0.437
μ_m	GPa	0.099
ϕ		0.405
T		1.796
κ_0	m^2	$1.504 \cdot 10^{-14}$

To verify that the mean model is a reasonable representation, we add the mean value parameters (Table 11) to the input values of C7 (Table 8) for a test run of the dry inversion. Thus, all poroelastic parameters of $\{\rho_s, K_s, \rho_f^{air}, K_f^{air}, \eta^{air}, K_m, \mu_m, \phi, T, \kappa_0, n_J\}$ are a priori known values of the inversion in addition to seismic input parameters of $\{V_S^{dry}, V_P^{dry}, \rho^{dry}\}$. Results of the corresponding predicted parameter values are presented in Table 12.

Comparing values in Table 8 and Table 12 confirms good agreement with seismic input parameter values for C7, which is also quantified by the low misfit value. VP_{slow} and QP_{slow} are constrained by conditions (4.3) and (4.4) indicated by their low values in Table 11. However, quality factors QP_{fast} and QS are too high.

Table 12. Predicted parameter values based on mean value model (Table 11) with corresponding value of misfit. *Red* background indicates parameters that contribute to the misfit function, whereas *grey* background indicates parameters that were not prescribed (see Table 8).

Symbols	Units	Values
VS^{pred}	m / s	250.01
VP_{fast}^{pred}	m / s	600.06
VP_{slow}^{pred}	m / s	0.274
ρ^{pred}	kg / m^3	1581.84
QS^{pred}		$1.2 \cdot 10^{10}$
QP_{fast}^{pred}		$1.1 \cdot 10^{12}$
QP_{slow}^{pred}		$6.0 \cdot 10^{-2}$
χ_{min}^2		$7.9 \cdot 10^{-7}$

To verify whether the mean value model can be considered reasonable from a physical point of view, we investigate if the obtained parameter values are plausible with respect to the material found at the site. The grain density of $\rho_s = 2658 kg / m^3$ and bulk modulus $K_s = 37 GPa$ are consistent with values of $2600 - 2700 kg / m^3$ and $33 - 38 GPa$ reported for silts and silty sands (e.g., Cheng 2016). Matrix parameters $K_m = 0.44 GPa$ and $\mu_m = 0.099 GPa$ are similar to values with $K_m = 0.27 GPa$ and $\mu_m = 0.1 GPa$ reported for coarse sands by Gregor *et al.* (2021). The value for porosity $\phi = 0.4$ is in the range of values for silt, silty sands, or lightly consolidated sands commonly reported with $0.3 - 0.5$ (e.g., Bardet *et al.* 1992, Cheng 2016). The value of Tortuosity $T = 1.8$ is between values found for coarse sands with ~ 1.25 (Gregor *et al.* 2021) and clays or quartzes with ~ 2.5 (e.g., Cheng 2016). The obtained value of permeability $\kappa_0 = 1.504 \cdot 10^{-14} m^2$ is, as expected, out of range for commonly found values for high permeable sediments as silts with values of $\sim 10^{-8} m^2$ (e.g., Bardet *et al.* 1992) or coarse sands (e.g., Gregor *et al.* 2021). However, comparatively low values can be found for e.g., clays, sandy clays, sandstones or limestones (Cheng 2016) but also lightly consolidated sands with $\sim 10^{-13} m^2$ (Masson & Pride 2006).

Lo & Sposio (2004) present investigations on Columbia fine sandy loam (63.2% sand, 27.5% silt, and 9.3% clay) saturated by an air-water mixture. Due to the clay content of their material, they obtain low permeability values similar to those in our model. The rest of their presented poroelastic parameter values are also in the same range of values found by our study. Only matrix parameter values of $K_m = 0.0083 \text{ GPa}$ and $\mu_m = 0.0039 \text{ GPa}$ are smaller than the ones of our model. Since there is no quantitative information about the pore saturation and depth, at which parameters were measured, provided, and we expect matrix parameters to be influenced by such conditions, we assume that these could be possible reasons for the difference in values. Therefore, a similar composition of sediments as found for Columbia fine sandy loam may be present at our investigated site. Here, geological, and geotechnical observations showed that the top 2m-thick layer of the soil column consists of artificial deposits (sandy and silty gravel with a small percentage of clay content) as described in subsection 1.2.3.1. Consequently, we conclude that from a physical point of view, it is reasonable to consider the determined model to describe the material at the site.

Overall, we conclude that we were able to determine a numerically and physically plausible set of poroelastic parameter values (Table 11), which can be considered representative material for the 2m-thick layer during the dry season.

4.3. Poroelastic inversion for the wet season

4.3.1. Choices of input parameter sets

The goal of the wet inversion is to obtain plausible models of poroelastic parameter values representing the material of the upper 2m thick layer during different stages of pore saturation for the wet season. First, we investigate the sensitivity of poroelastic output parameters considering 2 sets of input parameter values (see Table 13).

Table 13. Choices, C1 and C2, of input parameter sets for the inversion of poroelastic parameters. *Blue* background indicates directly constrained input parameter, *grey* background indicates unknown parameters and *red* background indicates parameters obtained by dry inversion.

Symbol	Units	Values	
		C1	C2
V_S^{wet}	m/s	155	
V_P^{wet}	m/s		
ρ^{wet}	kg / m ³		
ρ_s	kg / m ³	2654.5	2654.5
K_s	GPa	37.06	37.06
K_m	GPa		0.437
μ_m	GPa		0.0989
ϕ		0.404	0.404
T		1.661	1.661
κ_0	m ²	$1.575 \cdot 10^{-14}$	$1.575 \cdot 10^{-14}$
η_a	Pa s	$1.8 \cdot 10^{-5}$	
K_a	GPa	$0.145 \cdot 10^{-3}$	
ρ_a	kg / m ³	1.1	
η_w	Pa s	$1 \cdot 10^{-3}$	
K_w	GPa	2.25	
ρ_w	kg / m ³	997	
n_J	Pa s	8	
f_r	Hz	20	

For V_S^{wet} we use the value, which was determined by inversion of seismic observations during the wet season (Table 7). Analogously to the dry inversion, we consider $n_J = 8$ and the reference frequency $f_r = 20Hz$. We assume that the pore space is now filled by an air-water-mixture (i.e., $S = S_a + S_w$ with $S_w \neq 0$). Corresponding effective fluid parameter values $\{\eta, K_f, \rho_f\}$, saturation fractions $\{S_a, S_w\}$ and Brie exponent e are estimated by the inversion based on Eqs. (1.6) - (1.9). Hereby, fluid parameters of air and water enter the inversion as a priori known values which can easily be found in literature (e.g., Lo & Sposio 2004) as commonly accepted values.

For both choices C1 and C2, we use solid material parameters ρ_s and K_s found by the mean value model of the dry inversion since the solid component of the material does not change during seasons. Additionally, we use ϕ , T and κ_0 of the dry mean value model. These poroelastic input parameter values provided by the dry inversion help to better constrain the wet inversion. Therefore, we can avoid using Brocher's formulas to estimate additional seismic input parameters values for V_P^{wet} and ρ^{wet} .

For C1, we assume that matrix parameter values may change during the seasons. For example, the matrix of shaley sandstone is often softened when it is saturated with water due to the swelling of clay. Also, dried mud as a mixture of clay and water has larger matrix parameter values than clay which is fully saturated by water (Wang 2001). Therefore, with this choice we intuitively expect that the pore fluid interacts with the grains of the solid material in a way that it may soften or harden the matrix and changes its moduli.

For C2, we assume that matrix parameter values do not change during the seasons. A material like gravel, which could also be a possible constituent of the soil at the site, is not intuitively expected to have matrix parameters, which vary significantly between dry and wet seasons. Additionally, with we aim to consider as many possible input parameter values for the wet inversion as possible. Thus, we are interested to see if reasonable results can be obtained by the approach of fixed matrix parameter values of the dry inversion.

We performed preliminary inversions for both choices, C1 and C2, with seed value $s = 100$. Results of inverted poroelastic parameters obtained for both input sets are summarized in Table 14.

Table 14. Values of poroelastic parameters obtained for wet season for 2 input model choices (C1 and C2) for selected seed value $s = 100$. *Red* background indicates parameters that belong to a priori known values of the inversion (Table 13).

Symbols	Units	Values	
		C1	C2
S_a		0.47	0
S_w		0.53	1
e		28	14.3
K_m	<i>GPa</i>	39.9	
μ_m	<i>GPa</i>	0.0432	

Using Eqs. (1.26) - (1.31) and (1.7), we calculate wave speeds, quality factors and density corresponding to poroelastic parameters and using Eq. (3.9) we calculate the resulting misfit. The results for C1 and C2 are summarized in Table 15. We note that only the predicted S-wave speed value contributes to the misfit function, since the remaining seismic parameters are not a priori known.

Table 15. Summary of seismic parameters calculated from inverted poroelastic parameter values for C1 and C2 (Table 13). *Blue* background indicates parameters that contribute to the misfit function, whereas *grey* background indicates parameters that were not prescribed (see Table 8).

Symbols	Units	Values	
		C1	C2
VS^{pred}	<i>m / s</i>	155.00	223.11
VP_{fast}^{pred}	<i>m / s</i>	4714.25	1659.05
VP_{slow}^{pred}	<i>m / s</i>	9.62	1.44
ρ^{pred}	<i>kg / m³</i>	1797.94	1986.08
QS^{pred}		$4.9 \cdot 10^5$	$1.0 \cdot 10^6$
QP_{fast}^{pred}		$4.9 \cdot 10^5$	$1.6 \cdot 10^6$
QP_{slow}^{pred}		$2.9 \cdot 10^{-9}$	$4.6 \cdot 10^{-6}$
χ_{min}^2		0	0.193

First, we discuss the results of the inversion based on the input value set of C2 with fixed matrix parameter values. Here, the inversion did not lead to a reasonable value of estimated S-wave speed quantitatively resulting in a relatively large misfit value (see Table 15). In fact, the resulting value of $VS = 223m/s$ seems to be closer to the S-wave speed value of the dry season ($250m/s$). This indicates that the matrix parameters at the investigated site depend on the dry and wet seasons in a way which was intuitively anticipated by C1. The fluid, which is filling the pore space, is changing the surface energy of the rock material by physical and chemical interactions with the matrix (Wang 2001). Thus, the matrix of the material is softened during the wet season or hardened during the dry season. Therefore, matrix parameter values are changing with changing water saturation of the pores during the seasons, and C2 did not lead to reasonable parameter values, because fixed dry moduli were used.

To better explain this behavior, we can investigate the dependency of VS on S_w for C2 illustrated in Figure 16. We see the range of wave speed values of VS and VP_{fast} , which can be obtained based on the possible range of water saturation in the pores i.e., $S_w = [0,1]$. We assume a material described by poroelastic parameter values which were obtained by the dry mean value model (Table 11). It is important to look at this dependency since S_w is the only free parameter of the inversion for input set of C2 necessary for calculating VS .

Since VP_{fast} is dependent on fluid bulk modulus K_f , which itself depends on Brie exponent e (see eq. (1.8)), we show the variation of the fast P-wave speed with e and S_w by different colored curves in the left panel of Figure 16. The right panel of Figure 16 shows VS as a function of S_w . We note that the VS value ($250m/s$) for the air saturated condition (i.e., $S_w = 0$) corresponds to the dry season. VS decreases with increasing water saturation, as expected. However, the minimum value which can be obtained for pores fully saturated by water (i.e., $S_w = 1$) is $223m/s$. This is the same value which was estimated by the wet inversion based on C2 (Table 15). Therefore, the seismic constrained value of $155m/s$ cannot be obtained by any saturation condition based on poroelastic parameter values of the dry inversion that include matrix parameter values. Consequently, these values must be kept variable for the wet inversion as suggested by C1.

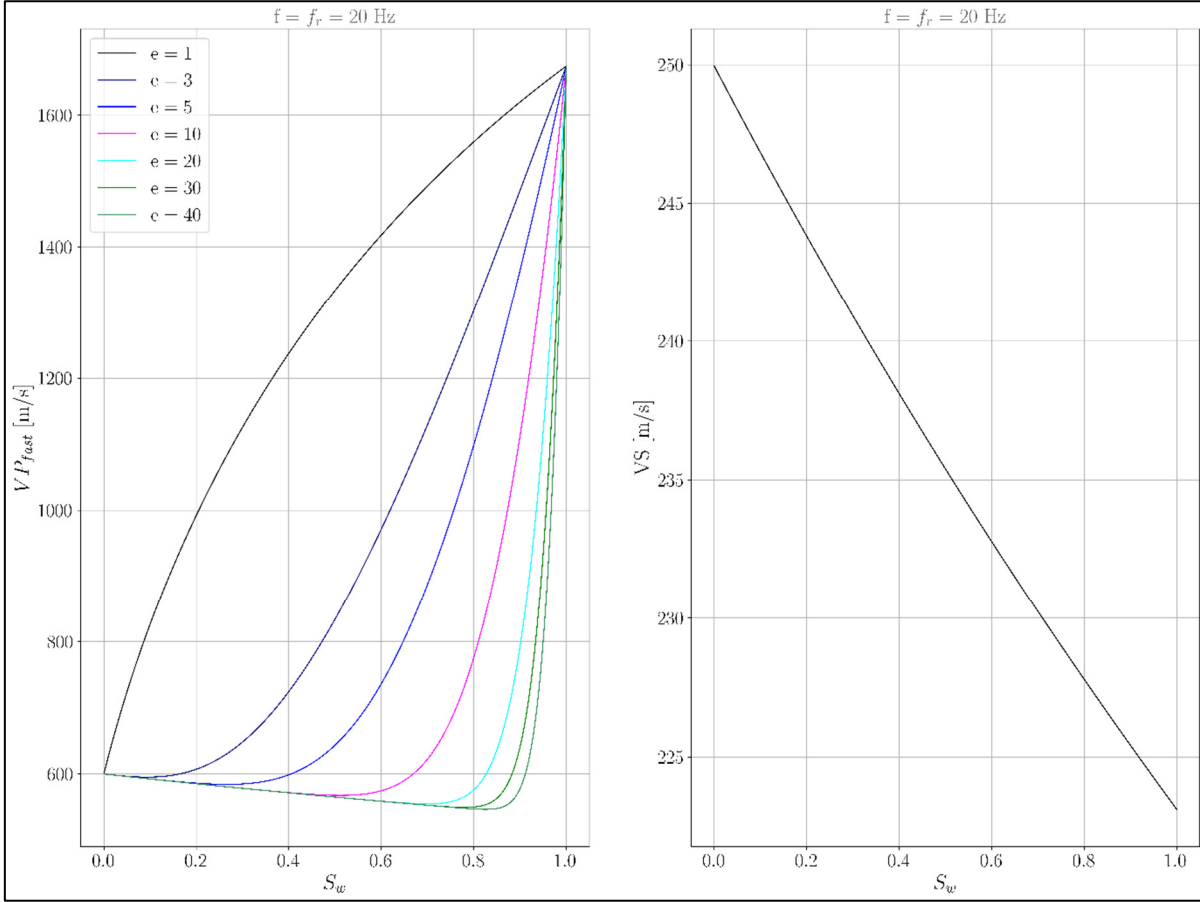


Figure 16. Saturation curves of VP_{fast} (left) and VS (right) for different Brie exponent values calculated based on poroelastic parameters of dry mean value model (Table 11).

Next, we will discuss results of the inversion based on the input value set of C1 without prescribed matrix parameter values. Although C1 predicts VS equal to the seismic constrained input value of $155m/s$, the value for predicted VP_{fast} of $\sim 4700m/s$ is too high for materials expected in the Argostoli basin. This is due to the not reasonable large value for K_m obtained by this inversion (Table 14). Since density must increase with increasing water content of the pores, the value of $\sim 1800kg/m^3$ seems reasonable compared to the one determined by the mean value model of the dry season $\sim 1600kg/m^3$. However, quality factors QP_{fast} and QS are smaller than the ones found for the dry season but still too high.

Due to the known dependency of output poroelastic parameters on varying seed values of the inversion, we will continue by considering various randomly selected seed values. For the dry inversion we found that K_m and μ_m had the narrowest scatter of values

and therefore, were the best constrained values by the inversion. However, for the wet inversion this might not be the case, since V_P^{wet} is not prescribed with an introduction of saturation into the inversion and thus, K_m may show a greater scatter of values due to its dependency on the fast P-wave. Therefore, we want to investigate further if a variety of values for K_m and corresponding VP_{fast} can be obtained, for which some fall into an admissible range of plausible values. A detailed discussion about this approach based on C1 will be presented in the following section.

4.3.2. Determination of models

We aim to find models of poroelastic parameters for different pore saturation conditions, which are in an admissible range of physically plausible values. First, we will try to invert reasonable saturation fractions of air and water corresponding to the set of input values of C1 based on various seed values. Thus, we will know under which possible saturation conditions the seismic S-wave speed value was constrained by observations. Additionally, the inversion will lead to the remaining missing poroelastic values of the Brie exponent and matrix parameters, and predicted seismic parameters of wave speeds, quality factors and density. This will improve our understanding and knowledge about wet inversions and shows us if/how plausible values of K_m and VP_{fast} can be obtained. Consequently, we aim to predict wave speed values corresponding to various saturation conditions of the ground. This further procedure can be summarized by the following steps based on C1:

- 1) Run the wet inversion for numerous randomly selected seed values.
- 2) Consider the lowest misfit model of each inversion.
- 3) Analyze correlations and interdependencies between parameters.
- 4) Investigate plausible physical constraints on models.
- 5) Predict wave speed values based on different ground saturation conditions.

We run the inversion for 100 randomly selected seed values s . For each inversion corresponding to 1 randomly selected seed value, we consider only the model of lowest misfit. This leads to 100 lowest misfit models. In Figure 17, 2D sections of the parameter space (S_a versus K_m , μ_m versus K_m , VP_{fast} versus K_m , e versus S_a , VP_{fast} versus S_a , S_a versus ρ , e versus ρ , VP_{fast} versus ρ) show the correlation between different

inverted and predicted parameter values for each model. The color of each model refers to its misfit value.

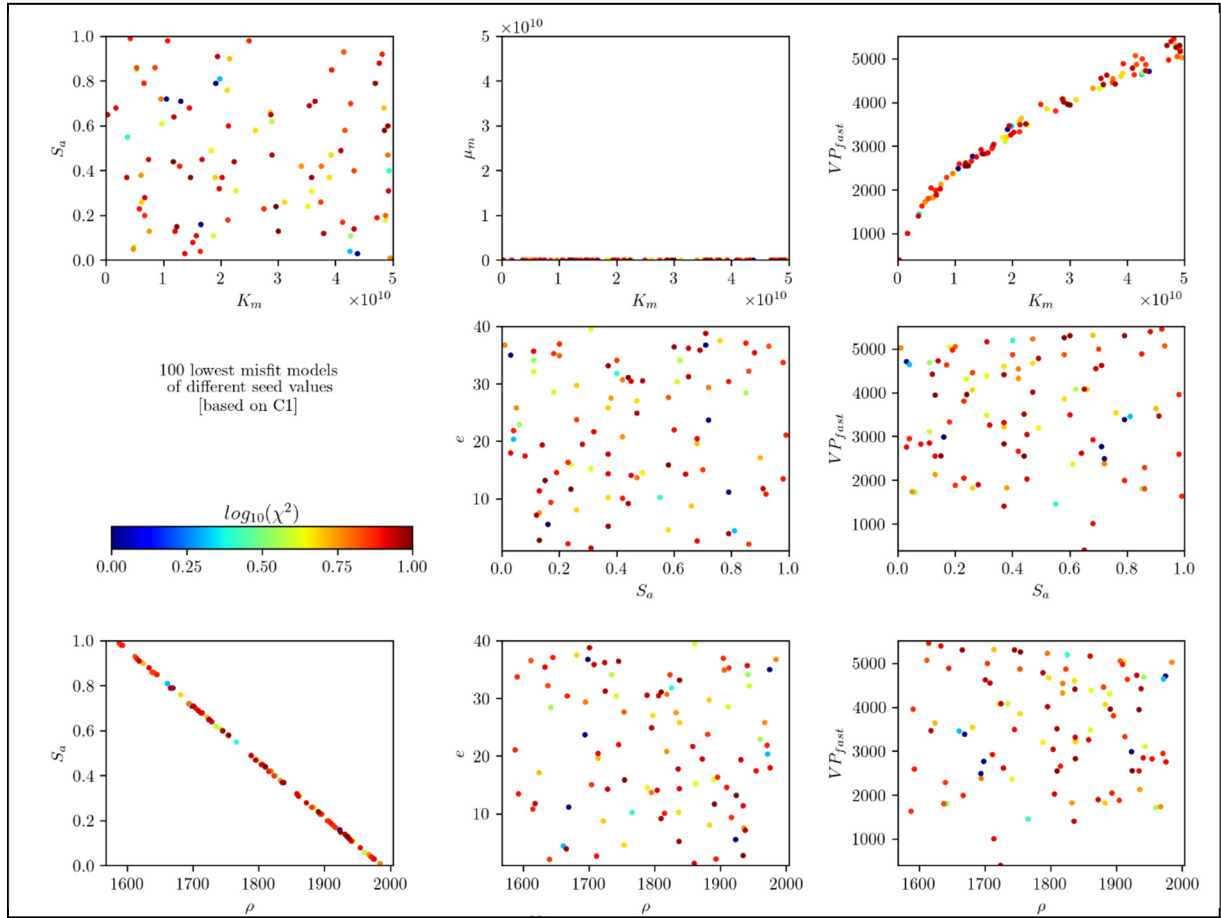


Figure 17. Lowest misfit models of 100 wet inversions corresponding to 100 randomly selected seed values.

Plots show the parameter values of each model in the parameter space. Ranges of the axes are set by lower and upper limits of parameters defined within the inversion algorithm (Table 2). Color of each model depends on the corresponding misfit value.

The inverted parameter with the narrowest scatter of obtained values is matrix shear modulus μ_m . All models are located at the bottom of the top middle 2D section which corresponds to a value of $\sim 0.04 GPa$. This is likely related to the fact that the value of S-wave speed is prescribed for the inversion and is strongly dependent on μ_m . This leads to an overall small range of possible matrix shear modulus values.

The increase of average bulk density of the proelastic medium with decreasing air saturation fraction (bottom left 2D section) is expected. The higher the water saturation of pore space, the larger the average density of the medium. For the air saturated condition

(i.e., $S_a = 1$), we obtain the corresponding density of the dry inversion (Table 12) providing a consistency of values.

The matrix bulk modulus K_m shows a wide scatter of obtained values over the whole considered range, as we anticipated (see previous subsection 4.3.1). Since the fast P-wave speed is not prescribed for the inversion and depends on the matrix bulk modulus, a variation of values for both, VP_{fast} and K_m , is reasonable. We see that with increasing matrix bulk modulus, also the fast P-wave speed increases (top right 2D section), which is expected.

Very interesting and unexpected to see is that K_m (and VP_{fast}) does not bound saturation S_a (top left 2D section). Consequently, small values of VP_{fast} can be achieved by small, as well as large values of S_a (middle right 2D section). Also, values of the Brie exponent do not bound this variation since there is no identifiable or visible relation between values of S_a and e (middle 2D section).

At this point we can make the first conclusion, that it is essentially impossible to find one model representing the wet inversion. Due to the dependency of VP_{fast} on K_m , we cannot determine a mean value model as we did for the dry inversion. Therefore, we aim to consider multiple models which cover the entire range of plausible values of VP_{fast} (and K_m).

Looking at all obtained values for $VP_{fast} = [0, 5500] m/s$, we now want to exclude models with unrealistically large wave speed values and only keep physically plausible ones. Therefore, we select those which fall into the admissible range of $VP_{fast} = [0, 2000] m/s$. This range is considered reasonable due to the average P-wave speed of 1500m/s in water (e.g., Aziman *et al.* 2016). Thus, we put a constraint on the matrix bulk modulus and decrease the prescribed upper limit value from 50 GPa (Table 2) to 10 GPa. The estimation of this newly prescribed range of K_m is based the interpretation of the upper right 2D section.

Additionally, we put a constraint on S_a and only look at models within a newly prescribed admissible range of $S_a = [0.5, 1.0]$ corresponding to a maximum water saturation of $S_w = 50\%$. As mentioned in subsection 1.1.1, there are three types of water content: gravity water, capillary water, and bound water. The largest part of the rainwater during the wet season is draining down to the water table (gravity water), the rest remains around the soil elements and can be evaporated but not drained due to its weaker linkage to the grain elements (capillary water). Since gravity water drains within a short amount of time and cannot be detected by the sampling rate of measurements, capillary water is expected to be responsible for the seasonal variation of the wave speeds. After personal communication with Dr. Hollender, capillary water is estimated to cause a maximum water saturation of the ground of $S_w = 50\%$, which defines the new limit values of saturation for further wet inversions.

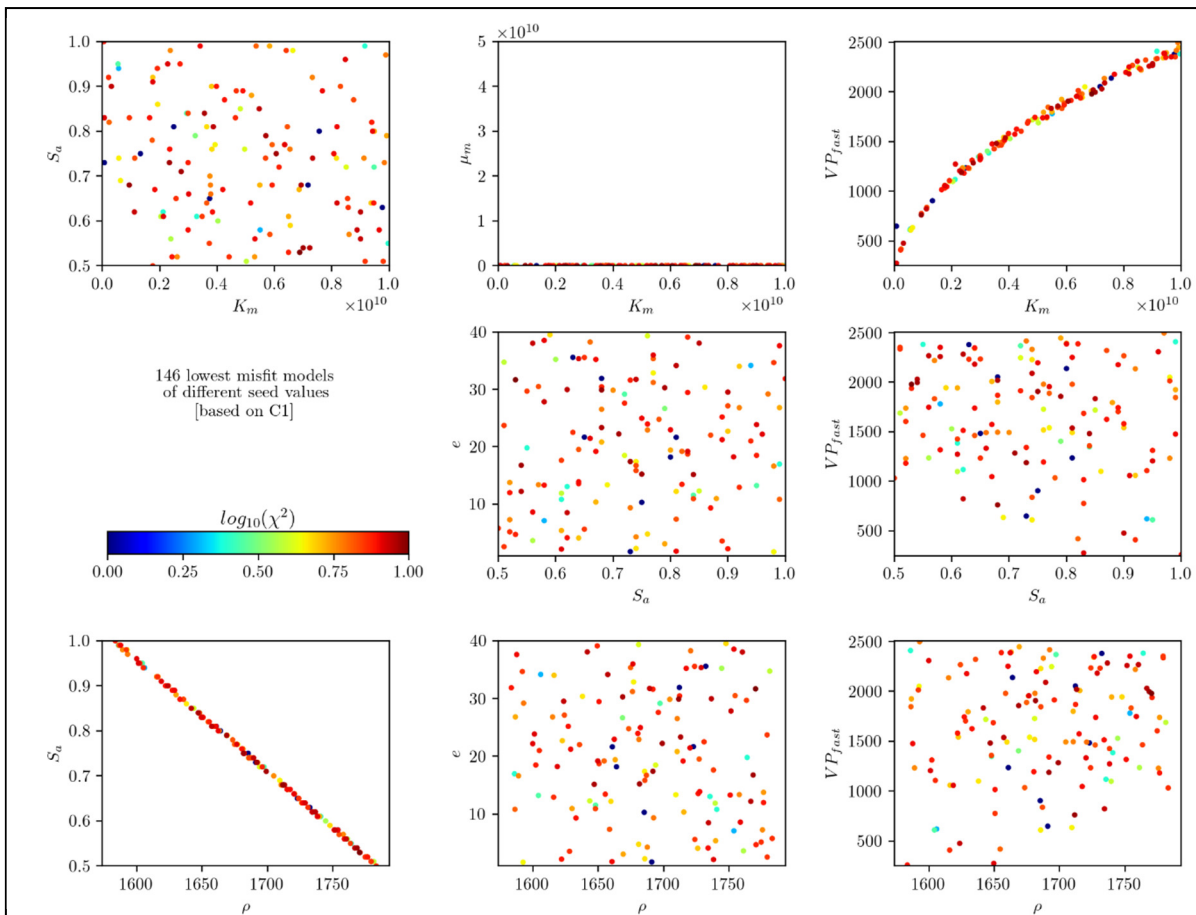


Figure 18. Lowest misfit models of 146 wet inversions for newly prescribed ranges of K_m and S_a .

Plots show the parameter values of each model in the parameter space. Ranges of the axes are set by lower and upper limits of parameters defined within the inversion algorithm (Table 2). Color of each model depends on the corresponding misfit value.

To increase the density of data points, we apply the constraints of VP_{fast} and S_a to the already given results of the first set of 100 inversions, but also perform a new set of 100 inversions based on randomly selected seed values with newly prescribed ranges for K_m and S_a . Thus, we increase the number of models in the range of interest providing possibly useful insights that are currently masked by a large number of models outside the range of interest. Results for a total number of 146 models are shown in Figure 18.

Although we increased the number of models in the range of parameters of interest, no further useful conclusions can be made at this point. Overall, all parameter values found by the wet inversion can be considered reasonable from a physical perspective. Looking at values of matrix bulk modulus, different types of sandstones can be associated with values of $K_m > 5 GPa$ presented by Cheng (2016). At the same time, there are also materials with reported values of $K_m < 1 GPa$ e.g., Abyssal red clay with $\sim 0.02 GPa$ (Cheng 2016) or Columbia fine sandy loam with an even smaller value of $\sim 0.008 GPa$ (Lo & Sposio 2004). For the Brie exponent a very commonly used value based on physical observations and experimental results is $e = 5$ (e.g., Carcione *et al.* 2006, Dupuy *et al.* 2016, Subagjo *et al.* 2018), but also other values used in literature can be found. Though, if we fixed the exponent to a specific value, this would not help with constraining models of reasonable fast P-wave speed, since there is still a dependence of VP_{fast} on saturation. After all, it remains challenging to choose additional physical criteria to select better models from worse ones.

However, for further investigations of plausible constraints, it should be considered if different parameters of one single poroelastic model can make up a combination of values describing a naturally realistic poroelastic material. Currently, there are no restrictions on physical plausibility of the selected combinations of parameters. Thus, a result of one inversion could be a model representing a poroelastic material with $\rho_f = 1 kg / m^3$ and $K_f = 100 GPa$, which are values that are incompatible in nature since a material with relatively low density would not be able to sustain such large stresses. Therefore, physical constraints and relations between different parameters on top of discussions with geologists are needed, which will be part of future investigations.

Also, attenuation of fast P- and S-waves has not been considered in more detail in the previous steps of our study. Comparing quality factors of both seasons in Table 12 and

Table 15, we can see comparatively smaller values during the wet season ($\sim 10^6$) than during the dry season ($\sim 10^{12}$). Relatively speaking, this makes sense, since fluid-matrix interactions in terms of fluid friction are causing a greater dissipation of energy and attenuation of seismic waves in water filled pores than in air filled pores (Winkler *et al.* 1982). However, this comparison of values must be seen critical, since QP_{fast} and QS in both seasons are still unrealistically high, which makes the difference in values almost irrelevant. One possible reason could be that attenuation is very highly sensitive to specific poroelastic parameters. Therefore, an analytical analysis of Eqs. (1.29) - (1.31) may help to identify parameters with stronger effect on the resulting quality factor values. However, due to complexity of Eqs. (1.29) - (1.31), it is unlikely that this problem can be solved analytically. Therefore, a numerical sensitivity study may be a more feasible approach. Starting with a set of known poroelastic parameters, Eqs. (1.29) - (1.31) can be used to calculate resulting values of quality factors for small perturbations of individual parameters or combination of parameters. Results of sensitivity analysis (analytical or numerical) may help to improve the results of the inversion. Therefore, the consideration of attenuation will and should be part of future investigations.

5 Conclusions

We investigated the seismically observed seasonal variation of the S-wave speed in the uppermost 2m-thick sedimentary layer in Argostoli, Cephalonia Island, Greece, due to rainfall-induced variation of water content in the layer. We assumed that the layer can be modelled as poroelastic medium and developed a computational program with an implementation of the Neighbourhood Algorithm to search for optimal poroelastic parameters. Inversions for both dry and wet seasons were performed based on the limited input information of seismic parameters (V_S , V_P and/or ρ) constrained by observations.

First, we searched for poroelastic models of the layer in the dry season, assuming full air saturation of pore space. All obtained models fit observations equally well with overall small relative errors of $< \pm 1\%$. We selected only physically plausible models with high attenuation and low speed of slow P wave. We represent the resulting set of models by mean values of poroelastic parameters. Results showed that the mean value model can be used as physically and numerically plausible model to represent the material during the dry season.

Next, we searched for poroelastic models of the layer in the wet season, assuming that the pore space is filled by an air-water mixture (without assuming a value of the water fraction). Our results indicate that the elastic parameters of the matrix change between the dry and wet seasons. However, because the wet inversion was constrained only by the observed S-wave speed, we obtained wide scatter of values of matrix bulk modulus and fast P-wave speed. Moreover, neither of the parameters helped to constrain water saturation level. Although material parameters of individual models obtained for the wet season seem physically plausible, we conclude that the results of the wet inversion cannot be represented by a single model.

We note that in our approach we did not consider physical constrains between different parameters. We expect that introducing physical correlations of material parameters together with additional constrains of material parameters based on discussions with geologists may help reducing the large scatter of values of the inverted material parameters for both the dry and wet seasons.

We also note that considering a non-zero volume of the bound water content could in principle improve the results, especially for the dry season. We considered the pore space to be filled by air during the dry season, whereas bound water is present within the pores

throughout the year. Consequently, considering that pore space filled by air-water mixture even during the dry season may be more appropriate.

Finally, we note that including quality factor for the fast P- and S-waves may help improving the results of the inversion as well. However, the inversion procedure may need adjustments based on insights obtained by an analytical and/or numerical analysis of sensitivity of attenuation to specific poroelastic parameters.

REFERENCES

- Arntsen, B., J.M. Carcione 2001. Short Note: Numerical simulation of the Biot slow wave in water-saturated Nivelsteiner Sandstone. *Geophysics* 66, 890-896.
- Auriault, J. L. 1980. Dynamic behavior of a porous medium saturated by a Newtonian fluid. *Int. J. Eng. Sci.* 18, 775-785.
- Aziman, M., Z.A.M. Hazreck, A.T.S. Azhar, D.S. Haimi 2016. Compressive and Shear Wave Velocity Profiles using Seismic Refraction Technique. *Journal of Physics: Conference Series* 710 (2016) 012011.
- Balam, R.I., U. Iturraran-Viveros, J.O. Parra 2018. Modeling Poroelastic Wave Propagation in a Real 2-D Complex Geological Structure Obtained via Self-Organizing Maps. *Pure Appl. Geophys.* 175, 2975-2986.
- Bardet, J.P. 1992. A Viscoelastic Model for the Dynamic Behavior of Saturated Poroelastic Soils. *Journal of Applied Mechanics* 59, 128-135.
- Bard, P.-Y., H. Cadet, B. Endrun, M. Hobiger, F. Renalier, N. Theodulidis, M. Ohrnberger, D. Fah, F. Sabetta, P. Teves-Costa, A.M. Duval, C. Cornou, B. Guillier, M. Wathelet, A. Savvaidis, A. Kohler, J. Burjanek, V. Poggi, G. Gassner-Stamm, H.B. Havenith, S. Hailemikael, J. Almeida, I. Rodrigues, I. Veludo, C. Lacave, S. Thomassin, M. Kristekova 2010. From non-invasive site characterization to site amplification: Recent advances in the use of ambient vibration measurements. In: Garevski, M., Ansal, A. (Eds.), *Earthquake Engineering in Europe*. Springer, Netherlands, Dordrecht, pp. 105-123. <https://doi.org/10.1007/978-90-481-9544->
- Berge-Thierry, C., A. Svay, A. Laurendeau, T. Chartier, V. Perron, C. Guyonnet-Benaize, E. Kishta, R. Cottureau, F. Lopez-Caballero, F. Hollender, et al. 2017. Toward an integrated seismic risk assessment for nuclear safety improving current French methodologies through the SINAPS@ research project, *Nucl. Eng. Des.* 323, 185–201.
- Biot, M. A 1956a. Theory of propagation of elastic waves in a fluid-saturated porous solid. I. Low frequency range. *J. acoust. Soc. Am.* 28, 168-178.
- Biot, M. A 1956b. Theory of propagation of elastic waves in a fluid-saturated porous solid. II. Higher frequency range. *J. acoust. Soc. Am.* 28, 179-191.
- Biot, M. A 1962a. Mechanics of deformation and acoustic propagation in porous media. *J. Appl. Phys.* 33, 1482-1498.
- Biot, M. A 1962b. Generalized theory of acoustic propagation in porous dissipative media. *J. acoust. Soc. Am.* 34, 1254-1264.

- Blanc, E. 2013. Theory of propagation of elastic waves in a fluid-saturated porous solid. PhD Thesis, Aix-Marseille Université.
- Brie, A., F. Pampuri, A. Marsala, and O. Meazza, 1995, Shear sonic interpretation in gas-bearing sands: SPE Annual Technical Conference, 30595, 701–710.
- Brocher, T.M. 2005. Empirical Relations between Elastic Wavespeeds and Density in the Earth's Crust. *Bulletin of the Seismological Society of America*, Vol. 95, No. 6, pp. 2081–2092.
- Brown, R. J. S. 1980. Connection between formation factor for electrical resistivity and fluid solid coupling factor in Biot's equations for acoustic waves in fluid-filled porous media. *Geophysics* 45, 1239-1319.
- Carcione, J.M., H.B. Helle, N.H. Pham 2003. White's model for wave propagation in partially saturated rocks: Comparison with poroelastic numerical experiments. *Geophysics* 68, 1389-1398.
- Carcione, J.M., S. Picotti, D. Gei, G. Rossi 2006. Physics and Seismic Modeling for Monitoring CO2 Storage. *Pure appl. Geophy.* 163, 175-207.
- Carcione, J.M., S. Picotti 2006. P-wave seismic attenuation by slow-wave diffusion: Effects of inhomogeneous rock properties. *Geophysics* 71(3), O1-O8.
- Carcione, J.M., J.E. Santos, C.L. Ravazzoli, H.B. Helle 2003. Wave simulation in partially frozen porous media with fractal freezing conditions. *Journal of Applied Physics* 94(12).
- Carione, J.M., G. Seriani 2001. Wave Simulation in Frozen Porous Media. *Journal of Computational Physics* 170, 676-695.
- Carcione, J.M., 2015. *Wave Fields in real Media, Wave Propagation in Anisotropic, Anelastic, Porous and Electromagnetic Media*. Elsevier, third edition.
- Cheng, A. H.-D., 2016. *Poroelasticity*. Springer.
- Coussy, Oliver 2004. *Poromechanics*. John Wiley & Sons, Ltd.
- Das, A., M. Sengupta 2021. Introduction to this special section: Rock physics. *The Leading Edge* (September 2021), Special Section: Rock physics.
- Das, V., T. Mukerji, G. Mavko 2019. Scale effects of velocity dispersion and attenuation (Q^{-1}) in layered viscoelastic medium. *Geophysics* 84, T147-T166.
- Dupuy, B., S. Garambois, J. Virieux 2016. Estimation of rock physics properties from seismic attributes - Part 1: Strategy and sensitivity analysis. *Geophysics* 81(3), M35-M53.

- Dupuy, B., A. Romdhane, P. Eliasson, H. Yan 2021. Combined geophysical and rock physics workflow for quantitative CO₂ monitoring. *International Journal of Greenhouse Gas Control* 106 (2021) 103217.
- Fliedner, M., S. Treitel, L. MacGregor 2012. Full-waveform inversion of seismic data with the Neighbourhood Algorithm. *The Leading Edge* (31:570-579), Special Selection: Seismic inversion for reservoir properties.
- Foti, S., F. Hollender, F. Garofalo, D. Albarello, M. Asten, P.Y. Bard, C. Comina, C. Cornou, B. Cox, G. Di Giulio, T. Forbriger, K. Hayashi, E. Lunedei, A. Martin, D. Mercerat, M. Ohrnberger, V. Poggi, F. Renalier, D. Sicilia, V. Socco 2018. Guidelines for the good practice of surface wave analysis: a product of the InterPACIFIC project. *Bull. Earthq. Eng.* 16, 2367-2420. <https://doi.org/10.1007/s10518-017-0206-7>.
- Garambois, S., C. Voisin, M.A. Romero Guzman, D. Brito, B. Guillier, A. Refloch 2019. Analysis of ballistic waves in seismic noise monitoring of water table variations in a water field site: added value from numerical modelling to data understanding. *Geophysical Journal International* 219, 1636-1647.
- Gist, A. G. 1994. Fluid effects on velocity and attenuation in sandstones. *J. Acoust. Soc. Am.* 96, 1158-1173.
- Gregor, D., P. Moczo, J. Kristek, A. Mesgouez, G. Lefeuve-Mesgouez, M. Kristekova 2021. Subcell-resolution Finite-difference Modelling of Seismic Waves in Biot and JKD Poroelastic Media. *Geophysical Journal International* (2021) 224, 760-794.
- Johnson, D., 2001, Theory of frequency dependent acoustics in patchy-saturated porous media: *Journal of Acoustical Society of America*, 110, 682–694, doi: 10.1121/1.1381021.
- Johnson, D. L., J. Koplik, R. Dashen. 1987. Theory of dynamic permeability and tortuosity in fluid-saturated porous media. *J. Fluid Mech.* 176, 379-402.
- Kelder, O., D.M.J. Smeulders 1997. Short Note: Observation of the Biot slow wave in water-saturated Nivelsteiner sandstone. *Geophysics* 62(6), 1794-1796.
- Knackstedt, M.A., C.H. Arns, W.V. Pinczewski 2003. Velocity-porosity relationships, 1: Accurate velocity model for clean consolidated sandstones. *Geophysics* 68(6), 1822–1834.
- Lemoine, G. 2013. Numerical Modeling of Poroelastic-Fluid Systems Using High-Resolution Finite Volume Methods. PhD Thesis, University of Washington.

- Lemoine, G.I., M.Y. Ou, R.J. Leveque 2013. High-resolution finite volume modeling of wave propagation in orthotropic poroelastic media. *SIAM J. Sci. Comput.* 35(1), B176-B206.
- Li, Y., L. Vernik, M. Chapman, J. Sarout 2019. Introduction to this special section: Rock physics. *Leading Edge* (May 2019), Special Section: Rock physics.
- Lo, W.C., G. Sposito, E. Majer 2004. Wave propagation through elastic porous media containing two immiscible fluids. *Water Resources Research* 41.
- Masson, Y.J., S.R. Pride, K.T. Nihei 2006. Finite-difference modeling of Biot's poroelastic equations at seismic frequencies. *J. Geophys. Res.* 111, B10305.
- Moczo, P., J. Kristek, P.Y. Bard, S. Stripajova, F. Hollender, Z. Chovanova, M. Kristekova 2018. Key structural parameters affecting earthquake ground motion in 2D and 3D sedimentary structures. *Bulletin of Earthquake Engineering* 16(6), 2421-2450.
- Moczo, P., D. Gregor, J. Kristek, J.d.l. Puente 2019. A discrete representation of material heterogeneity for the finite-difference modelling of seismic wave propagation in a poroelastic medium. *Geophys. J. Int.* (2019) 216, 1072–1099.
- Morochnik, V., J.P. Bardet 1995. Viscoelastic approximation of poroelastic media for wave scattering problems. *Soil Dynamics and Earthquake Engineering* 15, 337-346.
- Müller, T.M, B. Gurevich, M. Lebedev 2010. Seismic wave attenuation and dispersion resulting from wave-induced flow in porous rocks — A review. *Geophysics* 75(5), A147–A164.
- Nakata, N., R. Snieder 2012. Estimating near-surface shear wave velocities in Japan by applying seismic interferometry to KiK-net data. *Journal of Geophysical Research* 117, B01308.
- O'Connell, R.J., B. Budiansky 1978. Measures of dissipation in viscoelastic media. *Geophys. Res. Lett.* 5, 5-8.
- Plona, T. J., 1980. Observation of a second bulk compressional wave in a porous medium at ultrasonic frequencies. *Appl. Phys. Lett.* 36, 259.
- Press, W.H., S.A. Teukolsky, W.T. Vetterling, B.P. Flannery 1993. *Numerical Recipes in Fortran 77: The Art of Scientific Computing: Second Edition: Volume 1 of Fortran Numerical Recipes.* Cambridge University Press.
- Pride, S. R., 2005. Relationships between seismic and hydrological properties In Y. Rubin & S.S. Hubbard (eds.), *Hydrogeophysics*, 253-291, New York: Springer.
- Pride, S.R., J.G. Berryman, J.M. Harris 2004. Seismic attenuation due to wave-induced flow. *J. Geophys. Res.* 109, B01201.

- Protopapa, E., D. Papastamatiou, and G. Gazetas 1998. The IONIANET accelerometer array: early results and analysis, Proc. of the 11th European Conf. on Earthquake Engineering, Paris, France, September 1998, Balkema, Rotterdam, The Netherlands, ISBN: 90 5410 982 3.
- Roumelioti, Z., F. Hollender, P. Gueguen 2020. Rainfall-Induced Variation of Seismic Waves Velocity in Soil and Implications for Soil Response: What the ARGONET (Cephalonia, Greece) Vertical Array Data Reveal. *Bulletin of the Seismological Society of America* 110(2).
- Sahay, P.N. 2008. On the Biot slow S-wave. *Geophysics* 73(4), N19-N33.
- Sambridge, M. 1999. Geophysical inversion with a neighbourhood algorithm - I. Searching a parameter space. *Geophys. J. Int.* (1999) 138, 479-494.
- Sambridge, M. 1999. Geophysical inversion with a neighbourhood algorithm - II. Appraising the ensemble. *Geophys. J. Int.* (1999) 138, 727-746.
- Sbaa, S., F. Hollender, V. Perron, A. Imtiaz, P.-Y. Bard, A. Mariscal, A. Cochard, and A. Dujardin 2017. Analysis of rotation sensor data from the SINAPS@ Kefalonia (Greece) post-seismic experiment— Link to surface geology and wavefield characteristics, *Earth Planets Space* 69, 124, doi: 10.1186/s40623-017-0711-6.
- Schanz, M., 2009. Poroelastodynamics: Linear Models, Analytical Solutions, and Numerical Methods. *Appl. Mech. Rev.* 62(3), 030803.
- Schretter, C., I. Loris, A. Doms, P. Schelnkens 2014. Total Variation Reconstruction From Quasi-Random Samples.
- Sharma, M. D. 2007. Wave propagation in a general anisotropic poroelastic medium: Biot's theories and homogenization theory. *J. Earth Syst. Sci.* 116, 357–367.
- Smith, T.M., C.H. Sondergeld, C.S. Rai 2003. Gassmann fluid substitutions: A tutorial. *Geophysics* 68, 430-440.
- Stoll, R. D. 1977. Acoustic waves in ocean sediments. *Geophysics* 42, 715–725.
- Stoll, R.D., G.M. Bryan 1970. Wave attenuation in saturated sediments. *J. Acoust. Soc. Am.* 47(2), 1440-1447.
- Subagjo, I., B. Dupuy, J. Park, A. Romdhane, E. Querendez, A. Stovas 2018. Joint Rock Physics Inversion of Seismic and Electromagnetic Data for CO2 Monitoring at Sleipner. Conference & Exhibition Near Surface Geoscience 2018, Tu 24B 06.
- Svay, A., V. Perron, A. Imtiaz, I. Zentner, R. Cottreau, D. Clouteau, P.-Y. Bard, F. Hollender, and F. Lopez-Caballero 2017. Spatial coherency analysis of seismic ground

- motions from a rock site dense array implemented during the Kefalonia 2014 aftershock sequence, *Earthq. Eng. Struct. Dynam.* 46, no. 12, 1895–1917, doi: 10.1002/eqe.2881.
- Teja, A., and P. Rice, 1981, Generalized corresponding states method for viscosities of liquid mixtures: *Industrial and Engineering Chemistry Fundamentals*, 20, 77–81, doi: 10.1021/i100001a015.
- Theodoulidis, N., F. Hollender, A. Mariscal, D. Moiriat, P.-Y. Bard, A. Konidakis, M. Cushing, K.Konstantinidou, Z.Roumelioti 2018. The ARGONET (Greece) Seismic Observatory: An Accelerometric Vertical Array and Its Data. *Seismological Research Letters*.
- Turgut, A., T. Yamamoto 1988. Synthetic seismograms for marine sediments and determination of porosity and permeability. *Geophysics* 53, 1056-1067.
- Voigt, W. 1889. Über die Beziehung zwischen den beiden Elastizitätskonstanten isotroper Körper: *Annalen der Physik*, 274, 573–587, doi: 10.1002/(ISSN)1521-3889.
- Wang, Z. 2001. Y2K Tutorial Fundamentals of seismic rock physics. *Geophysics* 66(2). P. 289-412.
- White, J. E. 1975. Computed Seismic speeds and attenuation in rocks with partial gas saturation. *Geophysics* 40, 224-232.
- Wollner, U., J. Dvorkin 2018. Seismic-scale dependence of the effective bulk modulus of pore fluid upon water saturation. *Geophysics* 83, MR81-MR91.
- Yang, Q., W. Mao 2017. Simulation of seismic wave propagation in 2-D poroelastic media using weighted-averaging finite difference stencils in the frequency–space domain, *Geophys. J. Int.* 208, 148-161.
- Yeganeh, N., B. Fatahi 2018. Seasonal Effects on Seismic Performance of High Rise Buildings Considering Soil-Structure Interaction. Conference: The 16th European Conference on Earthquake Engineering (16ECEE). At: Thessaloniki, Greece.

ABSTRAKT

Die Geschwindigkeit der oberflächennahen Scherwelle (in der Seismologie oft als S-Wellengeschwindigkeit bezeichnet) ist einer der Schlüsselparameter, der die Amplituden der Bodenbewegungen bei Erdbeben beeinflusst und somit zu Standorteffekten beiträgt. Ihre Empfindlichkeit gegenüber saisonalen Schwankungen des niederschlagsinduzierten Bodenfeuchtigkeitsgehalts wurde durch seismische Beobachtungen für einen der erdbebenaktivsten Messstandorte Europas in Argostoli, Griechenland, quantifiziert.

Wir haben eine parametrische Untersuchung der dort beobachteten saisonalen Variation der S-Wellengeschwindigkeit in der Oberflächensedimentschicht durchgeführt. Unter der Annahme, dass die Schicht als poroelastisches Medium modelliert werden kann, war unser Ziel, mögliche poroelastische Materialien zu finden, die die beobachtete saisonale Schwankung der S-Wellengeschwindigkeit erklären könnten. Daher haben wir ein Programm entwickelt, das auf dem sogenannten Neighbourhood Algorithm basiert, um nach optimalen poroelastischen Parametern zu suchen, die das Material am Standort beschreiben. Basierend auf begrenzten Inputinformationen zu den Wellengeschwindigkeiten und der Dichte, die durch seismische Beobachtungen erlangt wurden, haben wir Inversionen sowohl für die Trocken- als auch für die Regenzeit durchgeführt.

Unsere Ergebnisse zeigen, dass das Material während der Trockenzeit unter der Annahme einer 100%igen Luftsättigung der Poren durch ein Modell dargestellt werden kann, das aus Mittelwerten poroelastischer Parameter besteht, die mittels zahlreicher Inversionen erhalten wurden. Die Materialparameter dieses Modells stimmen insgesamt mit den Parametern geologischer Materialien wie Schluff, schluffiger Sand, leicht konsolidierter Sand und grober Sand überein. Die Ergebnisse für die Regenzeit zeigen, dass sich die elastischen Parameter der Gesteinsmatrix zwischen der Trocken- und der Regenzeit ändern. Dies weist darauf hin, dass der sich ändernde Bodenfeuchtegehalt und die entsprechende porenfüllende Mischung aus Wasser und Luft durch physikalische und chemische Wechselwirkungen mit der Matrix eine Änderung der Oberflächenenergie des Gesteinsmaterials bewirken können. Die für die Regenzeit erhaltenen Materialparameter einzelner Modelle scheinen physikalisch plausibel und konsistent mit ähnlichen Materialien, wie sie für die Trockenzeit gefunden wurden. Aufgrund einer großen Streuung von Parameterwerten (verursacht durch begrenzte Inputdaten der Inversion) führte die

Inversion für die Regenzeit jedoch nicht zu einem bestimmten Modell, das als das am meisten bevorzugte angesehen werden könnte.

Schlagwörter: Poroelastisches Medium, seismische Wellengeschwindigkeit, saisonale Schwankungen, Argostoli in Griechenland, Neighbourhood Algorithm

ABSTRACT

The near-surface shear wave (S-wave) speed (often called S-wave velocity in seismology) is one of the key parameters impacting amplitudes of earthquake ground motion and thus contributing to site effects. Its sensitivity to the seasonal variation of rainfall-induced soil moisture content was quantified by seismic observations for one of the most earthquake active sites of Europe in Argostoli, Greece.

We performed a parametric investigation of this observed seasonal variation of the S-wave speed in the surface sedimentary layer at the site. Under the assumption that the layer can be modelled as a poroelastic medium, our goal was to find possible poroelastic materials that could explain the observed seasonal variation of the S-wave speed. Therefore, we developed a computational program based on the Neighbourhood Algorithm to search for optimal poroelastic parameters describing the material at the site. Based on limited input information on the wave speeds and density constrained by observations, we performed inversions for both dry and wet seasons.

Our results show that the material during the dry season, with the assumption of 100% air saturation of the pores, can be represented by a single model consisting of mean values of poroelastic parameters obtained from numerous inversions. Material parameters of this model are overall consistent with parameters of geological materials such as silts, silty sands, lightly consolidated sands, and coarse sands. Results for the wet season reveal that the elastic parameters of the matrix change between the dry and wet seasons. This indicates that the changing soil moisture content and corresponding pore-filling mixture of water and air may cause a change in surface energy of the rock material by physical and chemical interactions with the matrix. Material parameters of individual models obtained for the wet season seem physically plausible and consistent with similar materials as found for the dry season. However, due to a wide scatter of parameter values, caused by limited input data in the wet inversion, the wet inversion did not lead to one model that could be considered the most preferable.

Key words: Poroelastic medium, seismic wave speed, seasonal variation, Argostoli in Greece, Neighbourhood Algorithm